AGU PUBLICATIONS

Journal of Advances in Modeling Earth Systems

RESEARCH ARTICLE
10.1002/2016MS000743

Sources and pathways of the upscale effects on the Southern Hemisphere jet in MPAS-CAM4 variable-resolution simulations

Koichi Sakaguchi[1], Jian Lu[1], L. Ruby Leung[1], Chun Zhao[1], Yanjie Li[2], and Samson Hagos[1]

[1]Atmospheric Sciences and Global Change Division, Pacific Northwest National Laboratory, Richland, Washington, USA, [2]State Key Laboratory of Numerical Modeling for Atmospheric Sciences and Geophysical Fluid Dynamics, Institute of Atmospheric Physics, Beijing, China

Key Points:
- Regional refinement affects the Southern Hemisphere jet in a global variable-resolution model (MPAS)
- Increased precipitation in refined regions of the tropics changes meridional momentum transfer in the extratropics
- Grid refinement over the Asian Monsoon regions enhances cross-equatorial stationary Rossby waves

Supporting Information:
- Supporting Information S1

Correspondence to:
L. R. Leung,
ruby.leung@pnnl.gov

Citation:
Sakaguchi, K., J. Lu, L. R. Leung, C. Zhao, Y. Li, and S. Hagos (2016), Sources and pathways of the upscale effects on the Southern Hemisphere jet in MPAS-CAM4 variable-resolution simulations, *J. Adv. Model. Earth Syst.*, *8*, 1786–1805, doi:10.1002/2016MS000743.

Received 21 JUN 2016
Accepted 19 OCT 2016
Accepted article online 22 OCT 2016
Published online 11 NOV 2016

Abstract Impacts of regional grid refinement on large-scale circulations ("upscale effects") were detected in a previous study that used the Model for Prediction Across Scales-Atmosphere coupled to the physics parameterizations of the Community Atmosphere Model version 4. The strongest upscale effect was identified in the Southern Hemisphere jet during austral winter. This study examines the detailed underlying processes by comparing two simulations at quasi-uniform resolutions of 30 and 120 km to three variable-resolution simulations in which the horizontal grids are regionally refined to 30 km in North America, South America, or Asia from 120 km elsewhere. In all the variable-resolution simulations, precipitation increases in convective areas inside the high-resolution domains, as in the reference quasi-uniform high-resolution simulation. With grid refinement encompassing the tropical Americas, the increased condensational heating expands the local divergent circulations (Hadley cell) meridionally such that their descending branch is shifted poleward, which also pushes the baroclinically unstable regions, momentum flux convergence, and the eddy-driven jet poleward. This teleconnection pathway is not found in the reference high-resolution simulation due to a strong resolution sensitivity of cloud radiative forcing that dominates the aforementioned teleconnection signals. The regional refinement over Asia enhances Rossby wave sources and strengthens the upper level southerly flow, both facilitating the cross-equatorial propagation of stationary waves. Evidence indicates that this teleconnection pathway is also found in the reference high-resolution simulation. The result underlines the intricate diagnoses needed to understand the upscale effects in global variable-resolution simulations, with implications for science investigations using the computationally efficient modeling framework.

1. Introduction

General circulation models with variable-resolution (VR) grids hold promise for modeling regional climate [*Zarzycki and Jablonowski*, 2014; *Sakaguchi et al.*, 2015]. They simulate both global large-scale circulation and finer-scale processes over regions of interest while reducing the computational cost with coarser grid spacing across the rest of the globe. A potential advantage of the VR approach over limited area models is its ability to achieve two-way interactions across regions simulated at different resolutions (we use the term resolution to refer to horizontal grid resolution; also, we use this term interchangeably with grid spacing, recognizing the difference between grid spacing and the effective resolution [*Pielke*, 1991; *Skamarock*, 2004]) in a single, consistent framework [*Taylor and Fournier*, 2010; *Walko and Avissar*, 2011; *Ringler et al.*, 2011; *Skamarock et al.*, 2012; *Harris and Lin*, 2013; *Zarzycki et al.*, 2014]. Test simulations with realistic lower boundary conditions for the atmosphere have demonstrated added value by refining grid resolution [*Medvigy et al.*, 2011; *Harris and Lin*, 2014; *Zarzycki and Jablonowski*, 2014; *Sakaguchi et al.*, 2015; *Zarzycki et al.*, 2015]. Two-way interactions are also expected to affect model performance outside the high-resolution region by influencing large-scale circulations, as demonstrated by previous studies using VR models and two-way nested limited area models [e.g., *Lorenz and Jacob*, 2005; *Chen et al.*, 2011].

Inatsu et al. [2012] found that more realistic convective precipitation near the Philippines in a two-way nested limited area model led to improved circulation patterns over the western North Pacific outside the nested region. This remote effect was realized through an internal mode of variability that involves interactions between vorticity anomaly associated with latent heating and the background monsoonal circulation [*Hirota and Takahashi*, 2012]. *Medvigy et al.* [2013] provided some insights on possible remote effects of

Amazon deforestation on the hydroclimate of the western U.S. using the VR framework. The topography of the Andes was resolved better by regional grid refinement and produced stronger wind shear, which reinforced Rossby waves excited by a thermal contrast due to large-scale deforestation and propagating to the coarse-resolution domain. In both cases, the high-resolution effects on fine-scale features such as convection and topography first upscale locally to large-scale circulations (e.g., vorticity anomaly), which then propagate to remote locations via Rossby waves, possibly modulated by interactions with the background circulation. We define "upscale effects" as the influences of resolution due to regional refinement on large-scale circulations, both *locally* and *remotely*. By "large scale," we simply mean circulations with spatial scales larger than the target features of grid refinement, which are typically in the mesoscale range. As we shall see later, resolution effects appear not only inside the high-resolution region but also in the transition zone where grid spacing gradually changes from the finest to coarsest.

Sources for the upscale effects can be any features that are sensitive to grid resolution. Ideally the sources are the result of dynamical and physical processes that are expected to change with resolution when the models are able to better resolve certain forcings and/or processes. However, previous studies found that upscale effects could result from unphysical sensitivity of subgrid parameterizations to grid resolutions arising from assumptions on the statistical behavior of the processes [e.g., *Arakawa et al*., 2011] or structural uncertainty of process models [e.g., O'*Brien et al*., 2013]. *Rauscher et al*. [2013] and *Hagos et al*. [2013] studied the VR approach using the Model for Prediction Across Scales-Atmosphere (MPAS-A) [*Skamarock et al*., 2012; *Park et al*., 2013] coupled with the physics parameterizations of the Community Atmosphere Model version 4 (CAM4) [*Neale et al*., 2010] in aquaplanet simulations with prescribed sea surface temperatures (SSTs) [*Neale and Hoskins*, 2001]. With a circular grid refinement region centered at the equator in MPAS-CAM4, a localized precipitation maximum and associated diabatic heating anomaly appeared near the downstream boundary of the refined region, which excited equatorial Rossby waves to perturb the upper level circulations. Sensitivity experiments using the Held-Suarez dry test [*Rauscher et al*., 2013] and simulations comparing the CAM4 and CAM5 physics [*Zarzycki et al*., 2014] attributed the unphysical resolution dependence of the CAM4 moist physics as a source of the anomalous behavior. For grid refinement over the midlatitudes, MPAS-CAM4 produced localized maxima of eddy kinetic energy both upstream and downstream of the high-resolution region [*Rauscher and Ringler*, 2014]. The result from *Rauscher and Ringler* [2014] highlights the resolution effects on baroclinic eddies even though they are reasonably resolved at 100–200 km grid spacing.

As the next step to aquaplanet simulations in a hierarchical framework for model evaluation [*Leung et al*., 2013], *Sakaguchi et al*. [2015] analyzed MPAS-CAM4 simulations in the Atmospheric Model Intercomparison Project (AMIP) configuration with realistic geography and observed SST. In the refined regions, the AMIP VR simulations reproduced the spatial signatures of the global high-resolution simulations, which are dominated by regional forcings such as topography and their influence on regional circulations and clouds and precipitation. At the same time, visible upscale effects from the refined regions were identified. A particularly notable feature was a poleward shift of the Southern Hemisphere jet in austral winter (June-July-August). However, confounded by the spatially nonuniform and time-varying boundary conditions in the AMIP experiment, a direct mechanistic linkage of the upscale effects to specific processes in the regional refinement could not be immediately inferred.

As a major feature in the midlatitude circulation, the Southern Hemisphere jet plays a prominent role in shaping atmospheric processes such as blocking events and storm tracks [*Trenberth*, 1991]. Beneath the jet is the Southern Ocean, where extensive air-sea exchanges of momentum, energy, and trace gases take place under the influences of the Antarctic Circumpolar Current and the sea ice forming around Antarctica [*Godfrey and Rintoul*, 1998]. The upper level jet provides momentum to the surface wind, which exerts a direct forcing on the ocean current and sea ice dynamics. Sensitivity of the Southern Hemisphere jet to remote, local-scale processes may have a serious implication for long-term simulations using a VR approach, especially in fully coupled earth system models. This motivates more systematic analyses of VR simulations to identify the mechanisms behind the upscale effects found in *Sakaguchi et al*. [2015].

The overarching goals of this study are to provide a theoretical basis for scientifically rigorous applications of VR models that minimize upscale effects that are inconsistent with the reference high-resolution simulation and to pinpoint areas for future model improvement. To this end, we analyze three VR simulations, each targeting different regions for grid refinement. We do not attempt to explain every mechanism

Table 1. Descriptions of the MPAS-CAM4 Simulations

Experiment	Abbreviation	Grid Spacing (km)	Number of Cells Per Level	Center of Grid Refinement
Quasi-uniform low resolution	UR120	120	40,962	
Quasi-uniform high resolution	UR30	30	655,362	
Variable resolution, refinement over S. America	VR-SA	120–30	102,402	10°S, 60°W
Variable resolution, refinement over N. America	VR-NA			30°N, 90°W
Variable resolution, refinement over Asia	VR-Asia			30°N, 90°E

involved in the upscale effects, but rather focus on robust and illustrative examples, noting that the use of different physics parameterizations, different grid refinement regions, and different resolutions could favor or suppress certain mechanisms. The model experiments and diagnosis methods are summarized in section 2. In section 3, we first provide a global view of the upscale effects. The eastern Pacific is then examined in detail to demonstrate the link between the high-resolution tropical and the coarse-resolution extratropical regions. Two processes involved in the momentum flux that influences the jet are then diagnosed: high-frequency Rossby waves originating from the storm track and stationary Rossby waves from the tropics. The consistency of the upscale effects with the reference global high-resolution simulation and future work are discussed in section 4. A summary is given in section 5.

2. Methods

2.1. Model Experiments

We analyze the AMIP simulations of MPAS-CAM4 used in *Sakaguchi et al.* [2015] and an additional VR simulation, all performed using the prototype MPAS based on hydrostatic formulation with 26 sigma-pressure vertical levels (Table 1) [*Park et al.*, 2013]. Local mesh refinement of MPAS's unstructured grid is documented in *Ringler et al.* [2008] and *Ju et al.* [2011]. MPAS-VR simulations have been examined in the shallow-water test cases [*Ringler et al.*, 2011], baroclinic wave test cases [*Park et al.*, 2013], Held-Suarez and aquaplanet simulations [*Rauscher et al.*, 2013; *Martini et al.*, 2015], and AMIP simulations [*Sakaguchi et al.*, 2015]. MPAS-VR simulations were also compared to the nested grid approach of the Weather Research and Forecasting (WRF) model [*Skamarock et al.*, 2008] in the baroclinic wave test case [*Park et al.*, 2014] and aquaplanet simulations [*Hagos et al.*, 2013]. A general finding is that MPAS-VR is able to reproduce the dynamics of the global high-resolution simulation inside the refined grid domain without distorting wave propagation (baroclinic, equatorial, and gravity waves), but when the model is coupled to a full suite of physics parameterizations, the effects of resolution sensitivity of the moist processes are notable both inside and outside of the refined region.

Five AMIP simulations were run for 11 years from 1999 to 2009, with the last 10 years used in our analysis. These simulations are part of a hierarchical framework to evaluate the sensitivity of the hydrological cycle and extreme events to grid resolutions and dynamical cores [*Leung et al.*, 2013]. As in *Sakaguchi et al.* [2015], the AMIP case is chosen as the next level of complexity following the aquaplanet case and as a provisional step for our future work using coupled atmosphere-ocean simulations, which are under development. This study uses two AMIP simulations with quasi-uniform resolution grids at grid spacings of 120 km (UR120) and 30 km (UR30) and three VR simulations targeting different regions for grid refinement from 120 to 30 km resolution. In the first VR simulation (VRSA), the grid refinement is centered at (10°S, 60°W) and covers most of South America (Figure 1a) in a circular region with a radius of about 25° (Figure 1d). In the second VR simulation (VRNA), the high-resolution region covers a large part of North and Central Americas with its center at (30°N, 90°W). The quasi-uniform resolution and the above two VR simulations are the same as those analyzed in *Sakaguchi et al.* [2015]. An additional VR simulation (VRAsia) with grid refinement centering at (30°N, 90°E) over the Asian monsoon region is included in this study (Figure 1c). The simulations use a standard set of input parameters at all resolutions to eliminate effects of model tuning on resolution-dependent behavior of the models [*Leung et al.*, 2013]. Over land, the atmosphere model is coupled interactively to a land surface model (CLM4) [*Lawrence et al.*, 2011] while over the oceans, prescribed SST and sea ice covers are used [*Hurrell et al.*, 2008]. For more details of the experiments and models, readers are referred to *Sakaguchi et al.* [2015].

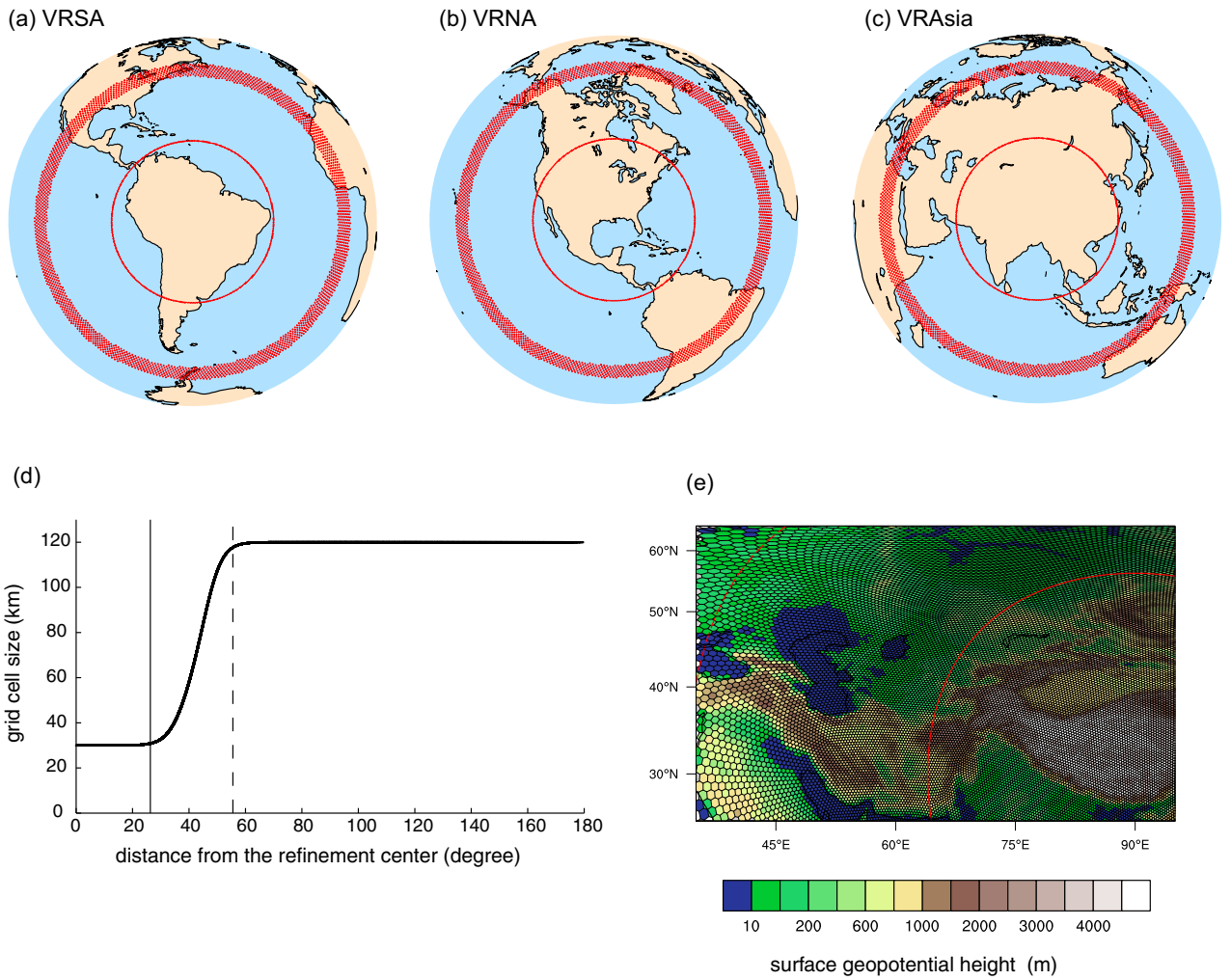

Figure 1. Configuration of variable-resolution grids: (a) center of the high-resolution region as placed over South America in VRSA, (b) North America (VRNA), and (c) Asia (VRAsia). Figure 1d shows how the grid cell size changes from the center of the refinement to the low-resolution domain. The solid vertical line (26°) corresponds to the inner circle in Figures 1a–1c, and the dashed line (56°) corresponds to the outer circle. (e) Topography in the VRAsia over the high-resolution, transition, and coarse-resolution regions.

2.2. Dynamical Diagnosis

Two diagnostic methods of eddy momentum flux associated with Rossby wave are used. Rossby wave propagation along the jet can affect the local atmospheric stability and momentum flux, and eventual wave breaking will result in the dissipation of momentum [e.g., *Farrell and Watterson*, 1985]. Before applying these methods, we separate the wind field into three time scales by bandpass filtering the 6-hourly model outputs to facilitate understanding of different processes involved in the momentum flux. The three time scales are high frequency or transient (2.5–6 days), low frequency (10–40 days), and stationary (longer than 40 days), similar to those in *Simpson et al*. [2014]. The contribution from the low-frequency component is found to be the smallest and will not be discussed.

The source and flow of the zonal momentum flux associated with Rossby waves are diagnosed as the flux of pseudomomentum, which is a quadratic function of wave amplitude. This quantity with a conservative property in a zonally uniform basic state is generally called wave activity [see e.g., *Vallis*, 2006; *Bühler*, 2009], so we use the terms pseudomomentum and wave activity interchangeably. The divergence of wave activity flux corresponds to a wave source where momentum flux converges to increase the mean (basic state) zonal wind speed. Convergence of the wave activity flux takes place where waves break and the mean wind decelerates. We use the flux calculation derived by *Takaya and Nakamura* [2001, equation C5] (for the pressure coordinates), in which pseudomomentum is defined by a linear combination of wave kinetic energy and enstrophy. Their wave activity flux, or **W** vector in their notation, is based on a quasi-geostrophic

potential vorticity equation that is linearized about a steady, nonuniform basic state wind. The **W** vector depicts the flux of wave activity along the group velocity of small-amplitude Rossby waves and is widely used to diagnose atmospheric teleconnections [e.g., *Wang et al*., 2014]. For the high-frequency component, our basic state is the climatological JJA stream function, and the deviations from it in each 6-hourly model output are used to calculate the **W** vector. In the case of the stationary flow, the basic state is the climatological JJA stream function of UR120, and the deviations from it in the other simulations are used to obtain the **W** vector.

To assess the possibility of cross-equatorial propagation of stationary Rossby waves, we use Rossby wave ray tracing that is also based on a steady, nonuniform basic state wind [*Li et al*., 2015; *Zhao et al*., 2015]. The ray tracing is derived from the barotropic, nondivergent vorticity equation without quasi-geostrophic assumptions, and can be considered as an extension to the work by *Schneider and Watterson* [1984] and *Watterson and Schneider* [1987], who added a zonal-mean (hence zonally uniform) meridional flow into the basic state, in contrast to a more traditional Rossby wave theory linearized about a basic state with zero meridional wind [e.g., *Hoskins and Karoly*, 1981]. In the approach taken by *Li et al*. [2015] and *Zhao et al*. [2015], both zonal and meridional basic flows are nonuniform in both latitude and longitude, making it appealing for diagnosing upscale effects because our grid refinement is local in the meridional and zonal directions. Their ray tracing starts with specifying a zonal wave number at the initial time, and the dispersion relationship is used to obtain the "local" meridional wave number and group velocity. The group velocity is then used to integrate the changes in the wave numbers in a Lagrangian manner. At each 1 h time step the group velocity is updated by the new wave numbers and the basic state in the new location. The same procedure is iterated for 30 days or until the total wave number ($K=\sqrt{k^2+l^2}$ where k and l are the zonal and meridional wave numbers, respectively) becomes greater than 40, representing wave breaking. Because the dispersion relationship involves spatially varying basic state variables, the wave numbers also change along the way. The basic state winds are spatially smoothed by retaining wave numbers of up to 11 after triangular truncation to focus on large-scale features that are most robustly captured by ray tracing. Readers are referred to *Li et al*. [2015] for more details.

3. Results

3.1. Global View of the Upscale Effects

The remote influence of grid refinement is shown in Figure 2. Figure 2a shows the JJA climatology of the 200 hPa level zonal wind from ERA-Interim [*Dee et al*., 2011]. Focusing on the Southern Hemisphere, the jet shows broad meridional structure representing both the thermally driven subtropical jet and the more poleward eddy-driven jet [*Bals-Elsholz et al*., 2001; *Nakamura and Shimpo*, 2004]. The split between the two is most clearly visible over Australia and the western Pacific. These features are reasonably reproduced in UR120, but biases such as the jet meandering too much equatorward over South America and too strong near Africa are also noted (Figure 2b). Reasonable agreement between the climatology of our MPAS-A simulations and ERA-Interim has already been shown by *Sakaguchi et al*. [2015] for a wide range of variables, even with no specific parameter tuning at each resolution. This model fidelity gives us confidence to diagnose the upscale effects based on theories and observations of large-scale circulations, particularly those in the Southern Hemisphere.

The general responses of the jet to increasing resolution are weakening and poleward shift as found in the aquaplanet experiments from the same model [*Rauscher et al*., 2013; *Lu et al*., 2015] and in other general circulation models although the jet intensity can be both stronger or weaker depending on models [*Pope and Stratton*, 2002; *Wan et al*., 2008; *Arakelian and Codron*, 2012] (also see *Lu et al*. [2015] for the related review and discussion). UR30 in the AMIP case shows somewhat different response in the Southern Hemisphere winter jet (Figure 2c). The jet is weaker in UR30 than in UR120 over the entire midlatitudes, and a stronger westerly is seen only over a portion of Antarctica. We will discuss this unexpected behavior of UR30 in section 3.3. The VR simulations exhibit features that are more in line with previous studies, namely the poleward shifts of the jet compared to UR120, particularly over the South American sector (Figures 2d–2f). In VRSA, the westerly wind is shifted not only inside the high-resolution and transition regions but upstream over the Pacific Ocean. A similar pattern is found in VRNA, but the magnitude and longitudinal extent are smaller than in VRSA (Figure 2e). The spatial pattern of the upscale effects is similar in VRAsia over South

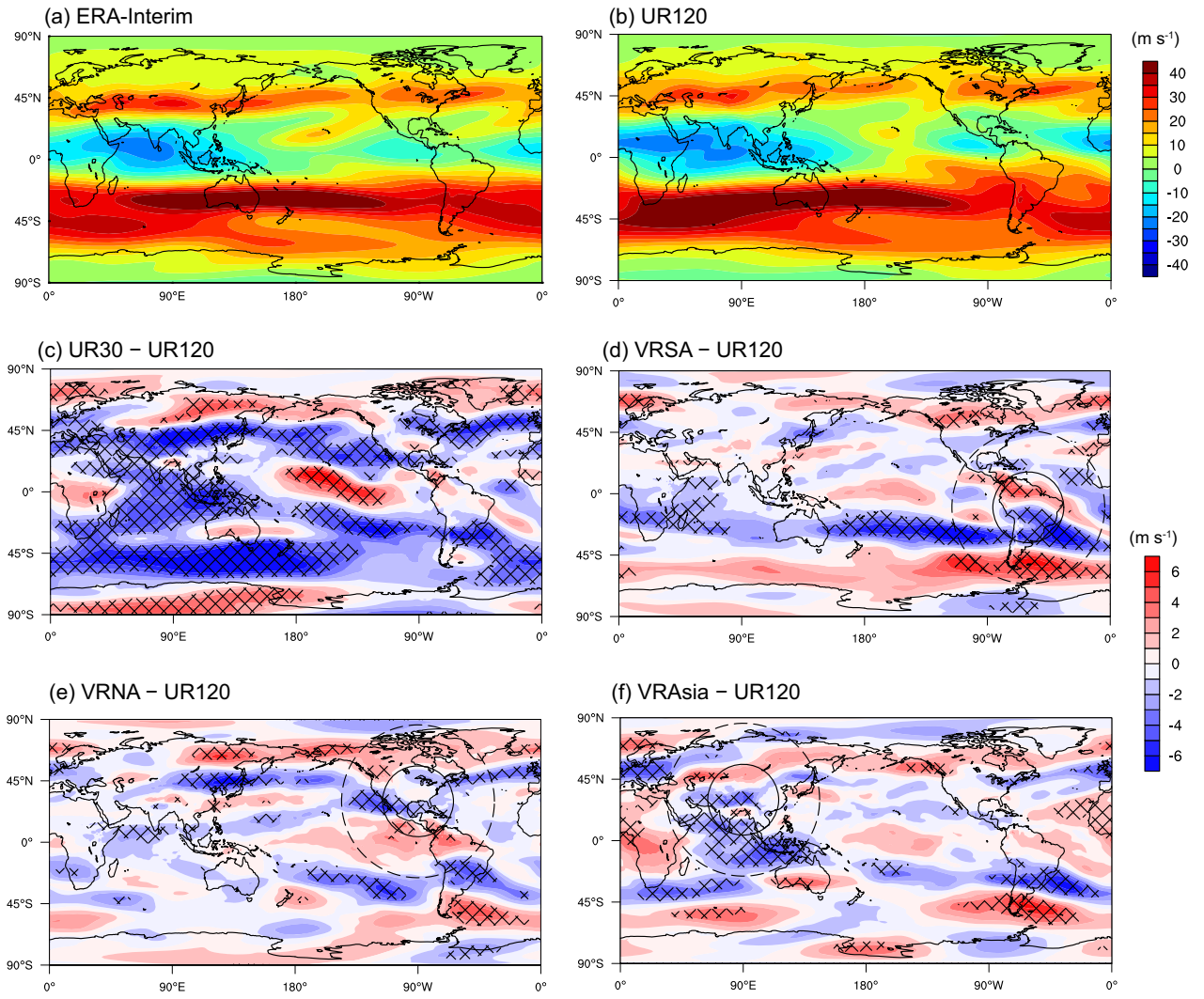

Figure 2. JJA mean zonal wind (m s^{-1}) at the 200 hPa level in (a) ERA-Interim and (b) UR120, and the difference between UR120 and (c) UR30, (d) VRSA, (e) VRNA, and (f) VRAsia. The crosshatch in this and other figures indicates the grid cells with statistically significant difference at the 5% level based on two-sided Student's *t* tests.

America, despite the grid refinement being quite far from there (Figure 2f). Many of the *p* values obtained in the local hypothesis testing at grid points (the null hypothesis of no difference between the VRs and UR120) are strong enough to pass the global (field) significance at $\alpha = 0.05$ level, according to the False Discovery Rate criterion [*Ventura et al.*, 2004; *Wilks*, 2006]. This is also the case for other variables presented below. The local (grid point level) hypothesis testing takes into account the influence of lag-one autocorrelation on the sample variance [*Zwiers and von Storch*, 1995].

The JJA mean precipitation in UR120 is shown in Figure 3 along with the climatology from GPCP [*Huffman et al.*, 2009]. Characteristics of the JJA precipitation are reasonably captured by UR120 although there exists some regional discrepancies that are common among global models [*Flato et al.*, 2013], such as the double-ITCZ over the western Pacific and underestimation of the ITCZ maxima over the eastern Pacific and Atlantic Oceans. The difference plot between UR30 and UR120 depicts the sensitivity of the simulated precipitation to resolution (Figure 3c). Precipitation increases with increasing resolution over the local maxima in the monsoon regions and the ITCZ, typically by 15–20% (about half or less of the bias relative to GPCP), with compensating decreases nearby, such as the Indian Ocean and central equatorial Pacific. This resolution dependency is similar to those documented in *Bacmeister et al.* [2014] using the default finite-volume dynamical core with the CAM4 and CAM5 physics. All the VR simulations display similar tendency as UR30, not only inside the high-resolution regions but also in the transition regions, demonstrating the large

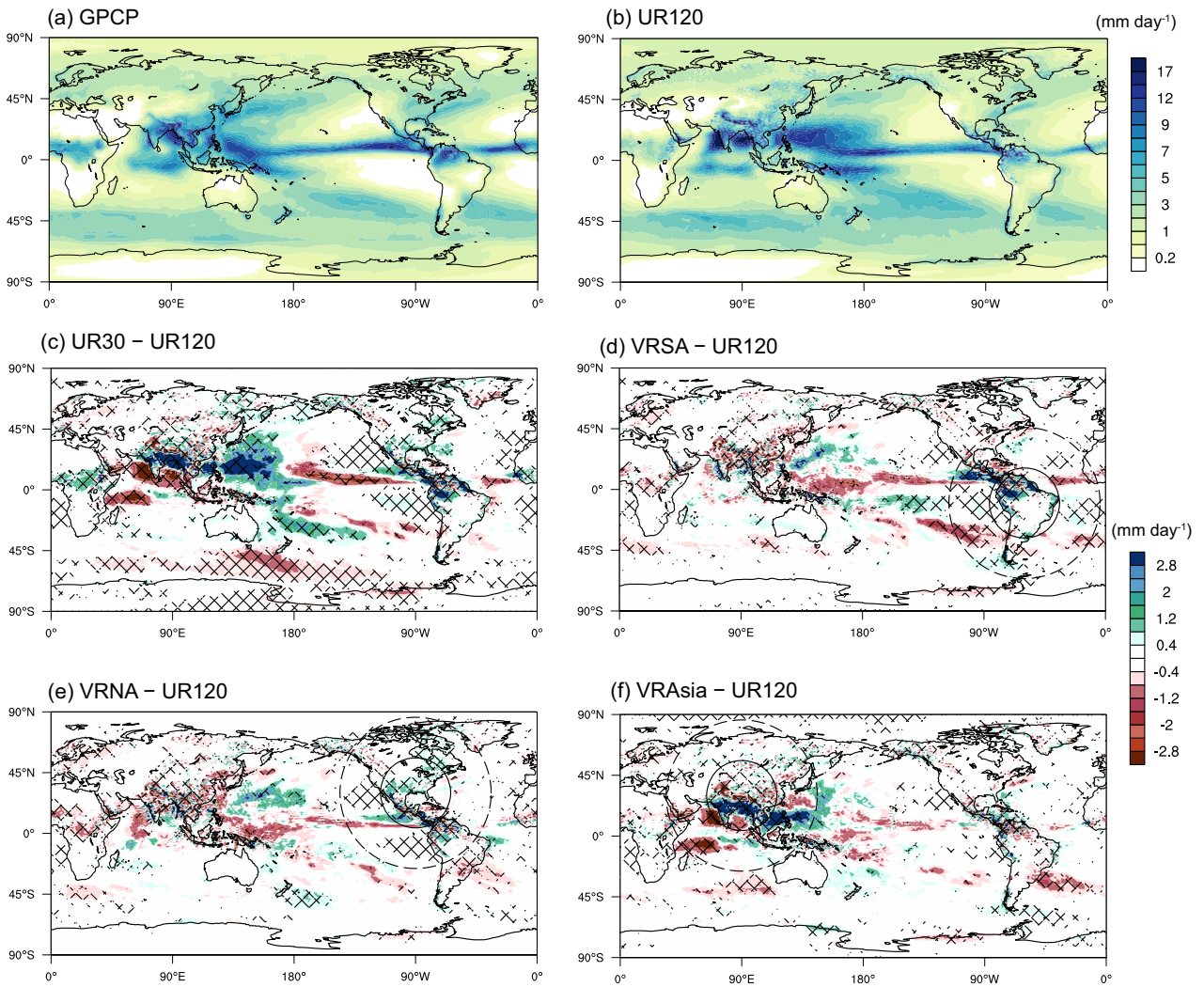

Figure 3. Same as Figure 2 but for precipitation (mm d^{-1}) with (a) from GPCP.

sensitivity of moist processes to resolution (Figures 3d–3f). As a result, the VR simulations have different distributions of diabatic heating from that in UR120. Precipitation changes are also noticeable outside the high-resolution regions due to global conservation of energy and moisture, but most of the changes are not statistically significant at the 5% level.

The consequential difference in latent heat release is reflected on the upper level divergent circulation. In JJA, the global monsoon circulations (particularly that of the Asian monsoon) dominate the overall pattern (Figures 4a and 4b) [*Hoskins and Wang*, 2006; *Trenberth et al.*, 2006]. UR30 intensifies the divergent circulation everywhere compared to UR120 (Figure 4c). The VR simulations reproduce some of the enhanced divergence as in UR30, but the spatial extent and magnitude are smaller (note the different color and velocity scales in Figure 4c and in Figures 4d–4f). In VRSA, stronger divergence (negative velocity potential) relative to UR120 is created over the eastern Pacific ITCZ and the central Andes where precipitation is greater in VRSA as well. This increased divergence induces compensating convergence locally to its east over the southwestern Atlantic and to its west over the South Pacific. Looking at the difference between VRNA and UR120, we find a similar pattern as in the case of VRSA but with somewhat weaker amplitude (Figure 4e). The muted response in VRNA is expected since VRNA does not increase precipitation relative to UR120 by as much as VRSA over the eastern Pacific ITCZ and the central Andes (Figure 3e). VRAsia enhances the divergence-convergence dipole in the entire Eastern Hemisphere such that the easterly as well as the cross-equatorial wind components become stronger near 90°E (Figure 4f). A divergent anomaly is also noticeable

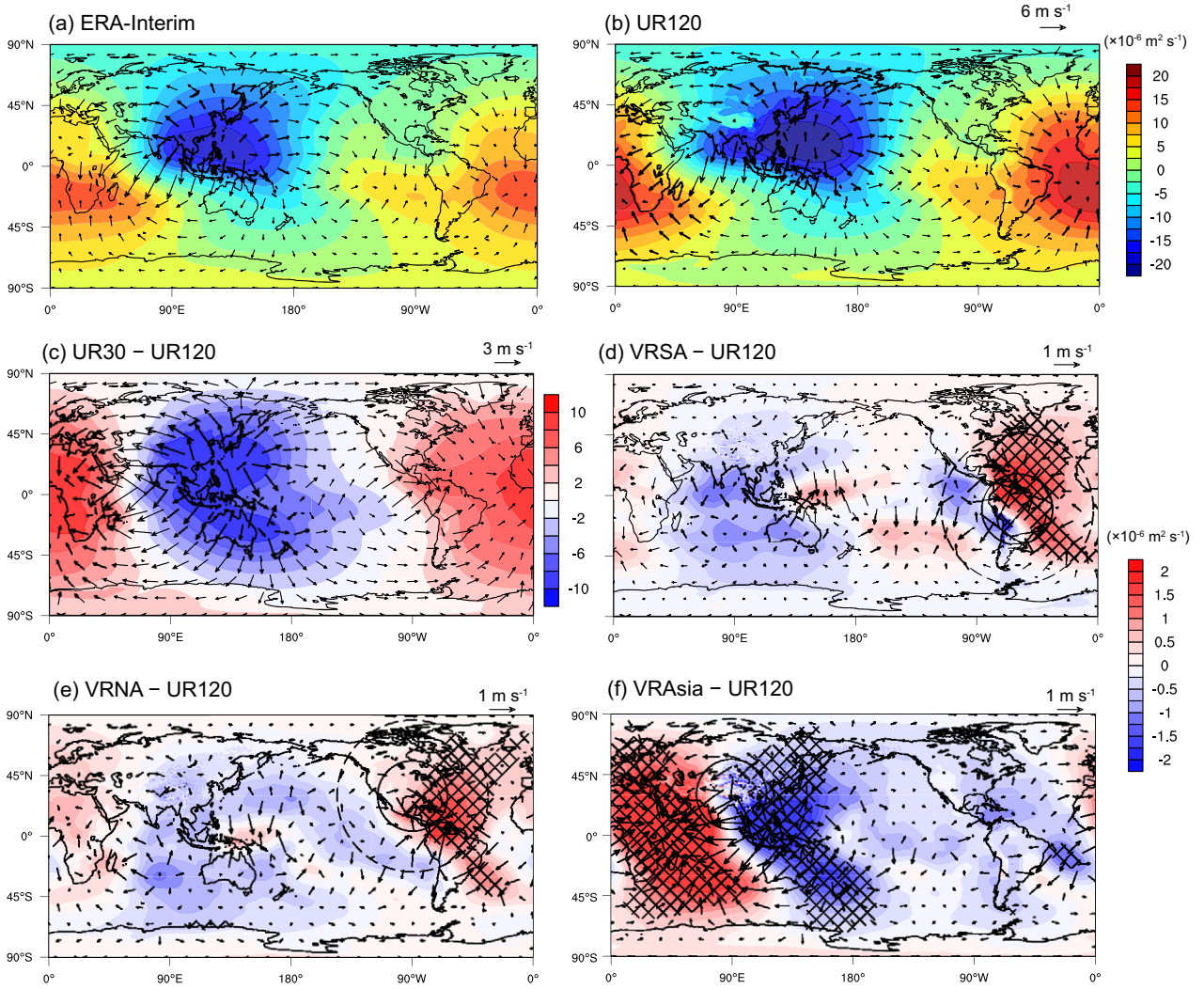

Figure 4. Same as Figure 2 but for velocity potential (color, $m^2\ s^{-1}$) and divergent component of the wind (arrows, $m\ s^{-1}$). In Figure 4c, the color scale and arrow scale are different from Figures 4d to 4f, and the crosshatch is not shown for visual clarity because all the colored contours are statistically significant at the 5% level.

over the southwestern Atlantic, which creates a wave-like pattern with the convergence anomaly to the east of South America. Later we will show that this location is actually a preferred path for Rossby waves traveling from the midlatitudes in VRAsia. In fact, all VR simulations show preferred convergence anomalies over the western tropical Pacific, the central-eastern South Pacific, and the southwestern Atlantic, which are all statistically significant (not shown, but most of them are clearly visible in velocity potential shown in Figure 4). The anomalies in the latter two locations coincide with the slower westerly jet in VRs relative to UR120, hence suggestive of some link between the resolution-sensitivity in the tropical precipitation and the midlatitude dynamics, which we focus on in the next section.

3.2. ITCZ Diabatic Heating and Subtropical Subsidence

Here we use the eastern Pacific in VRSA and UR120 as an illustrative example for a link between the divergent circulation from the tropics and the momentum balance in the subtropics/midlatitudes as a pathway for the upscale effects. The reason we choose this region is that the anomalous circulation (difference between the VRs and UR120) has a smaller zonal component, which simplifies the analysis. Generally similar results are also obtained in the VRNA versus UR120 comparison, but the signal is not as robust. Hence, for the following analyses, the VRNA results are only provided in the supporting information.

Taking a seasonal (JJA) and zonal average over the eastern Pacific (80°W–130°W) in UR120, two cells of meridional circulation are apparent in the lower latitudes of the Southern Hemisphere (Figure 5a). The

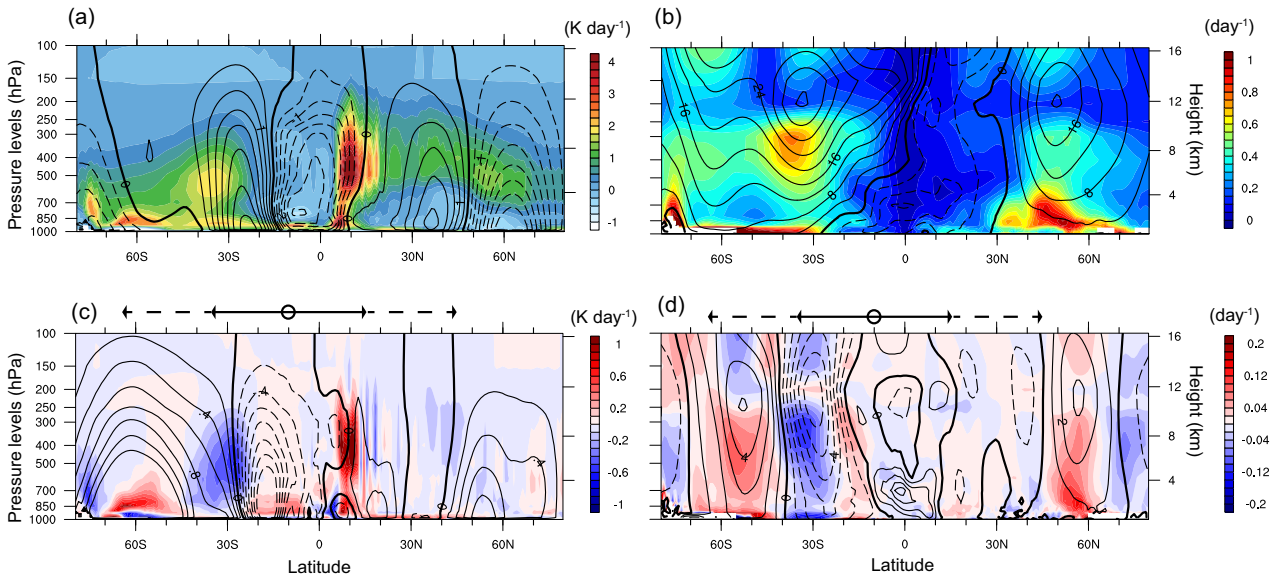

Figure 5. Seasonal (JJA) and zonal (80°W to 130°W covering the eastern Pacific) mean cross sections of variables showing the tropics-extratropics teleconnections: (a) condensational heating (color, K d^{-1}) and meridional stream function (line contour, kg s^{-1} multiplied by 10^{-11}) from UR120; (b) Eady growth rate (color, day^{-1}) and zonal wind (line contour, m s^{-1}) from UR120. (c and d) The differences between VRSA and UR120 in the same variables as Figures 5a and 5b, respectively. The dashed line contours represent negative values. The horizontal lines above Figures 5c and 5d indicate the latitudinal range of the grid refinement: the solid line is for the high-resolution latitudes, dashed lines are for the transition region, and the circle is for the center of the high-resolution region.

ascending branch of the equatorial cell, which we call the local Hadley cell, is collocated with the condensational heating maximum in the ITCZ near 10°N. Another ascending motion is found near 35°S together with the heating maximum from the storm track and possibly from the easternmost part of the South Pacific Convergence Zone [*Vincent*, 1994]. The jet core appears near 35°S at the 200 hPa level (Figure 5b). This climatological state reflects the most baroclinically unstable region right beneath the jet core, indicated by the color shading of the Eady growth rate

$$\sigma_{BI}=0.31\frac{f}{N}\frac{\partial u}{\partial z} \tag{1}$$

where f is the Coriolis parameter and N is the Brunt-väisälä frequency [*Lindzen and Farrell*, 1980; *Hoskins and Valdes*, 1990]. The latitudinal position of this maximum baroclinicity is consistent with observation [*Karoly et al.*, 1998], and a strong meridional temperature gradient exists at the same latitudes as the thermal wind balance implies (as indicated from the prescribed SST, Figure 6). In VRSA, the condensational heating in the ITCZ and the Peruvian Andes is intensified compared to UR120, and at the same time, the local Hadley cell is expanded to the south as shown by the difference in the meridional stream function (Figure 5c). This expansion clearly plays a role in the dynamics of the westerly jet because the cell's stronger and shifted descending branch is collocated with the weakened convective activities (Figure 5c) and reduced σ_{BI} (Figure 5d).

The stronger northerly wind at the upper level should accelerate the westerly jet through the Coriolis torque, according to the following zonal momentum equation [e.g., *Simpson et al.*, 2014]

$$\begin{aligned}\frac{\partial u}{\partial t}\sim 0 \sim fv-\frac{1}{a\cos\phi}\frac{\partial\Phi}{\partial\lambda}-\frac{1}{a\cos^2\phi}\frac{\partial(uv\cos^2\phi)}{\partial\phi}-\frac{1}{a\cos\phi}\frac{\partial(uu)}{\partial\lambda}-\frac{\partial(u\omega)}{\partial p}+F_u\\ =fv_{ag}-\frac{1}{a\cos^2\phi}\frac{\partial(uv\cos^2\phi)}{\partial\phi}-\frac{1}{a\cos\phi}\frac{\partial(uu)}{\partial\lambda}-\frac{\partial(u\omega)}{\partial p}+F_u\end{aligned} \tag{2}$$

where a is Earth's radius, ϕ is latitude, λ is longitude, Φ is geopotential, and F_u collectively represents the subgrid-scale forcings such as friction and momentum transfer by deep convection [*Richter and Rasch*, 2008]. In the second line, the Coriolis force and the height gradient terms are combined as the ageostrophic Coriolis torque. The sum of all the forcings should, on average, be nearly zero for the seasonal climatology,

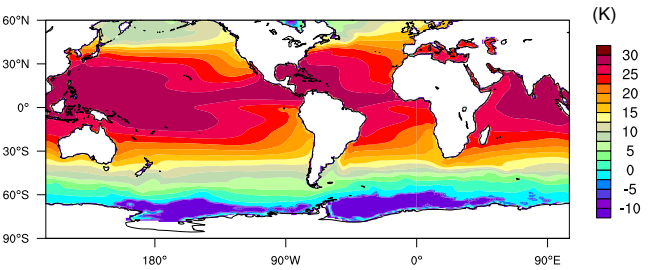

Figure 6. Spatial pattern of the JJA-mean SST forcing used in our simulations.

and it is indeed the case for our MPAS simulations except for the boundary layer and near the equator, since F_u is not included in our diagnosis (not shown). Figure 7 shows the difference averaged over the eastern Pacific (80°W–130°W) between UR120 and VRSA in the Coriolis torque, *uv* flux divergence, *uu* flux divergence, and the sum of the three flux divergence terms (*uv*, *uu*, and $u\omega$). The $u\omega$ term is much smaller than the others and hence not shown. As expected, the Coriolis torque is greater in VRSA at the core latitude of the subtropical jet (Figure 7a). The contributions from the *uv* and *uu* flux terms are opposite to each other over most of the region (Figures 7b and 7c), but the magnitude of the negative *uu* divergence is stronger than the opposing *uv* divergence term near the subtropical jet core, leading to the net negative contribution to the zonal momentum budget. The strong forcing from the longitudinal divergence of the *uu* flux also implies the upstream or downstream influence on the regional momentum budget. Overall, the poleward-shifting pattern in the total momentum flux divergence over the latitudes between 20°S and 40°S (Figure 7d) and the similar shift in the maximum baroclinicity conform to the intimate relationship between baroclinic waves and momentum transfer [*Trenberth*, 1986; *Held and Hoskins*, 1985]. That is, baroclinic disturbances excite Rossby waves, and their propagation and subsequent dissipation constitute a momentum transfer to the source region.

We note that this budget analysis on quasi-equilibrium states may not be used to isolate the cause and response. However, a priori knowledge of the resolution sensitivity of convective rain [*Rauscher et al.*, 2013; *Sakaguchi et al.*, 2015] suggests that the diabatic heating change in the ITCZ and over South America is likely the dominant cause for the differences shown in this section. In the budget analysis, the change in the Coriolis torque can be explained by those in the local Hadley cell. Now we turn our attention to the sources of the other major forcing, the eddy momentum flux.

3.3. Baroclinic Waves From the Storm Track

We first present the result regarding the momentum flux associated with the transient flow. The spatial pattern of σ_{BI} at 400 hPa in UR120 is shown in Figure 8a. The regions of high σ_{BI} are mostly aligned with the

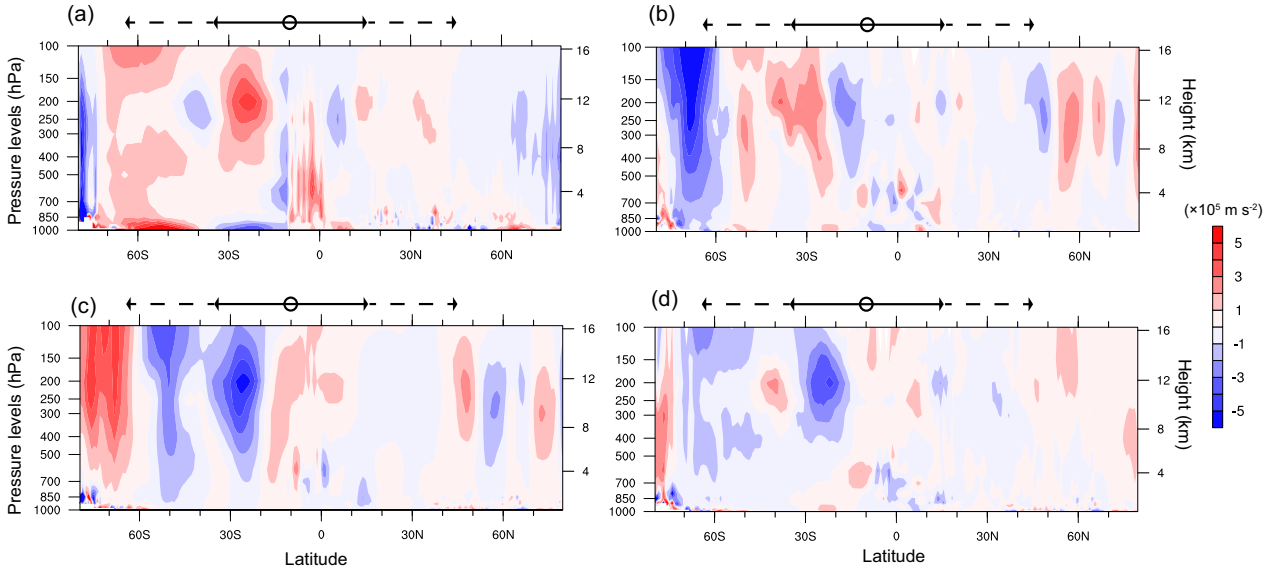

Figure 7. Difference in the four terms in the zonal momentum equation (m s^{-2}) between VRSA and UR120 after seasonal (JJA) and zonal averaging over the Eastern Pacific (80°W–130°W): (a) ageostrophic Coriolis torque, (b) *uv* flux divergence, (c) *uu* flux divergence, and (d) the sum of *uv*, *uu*, and $u\omega$ flux divergence terms. The sign of each term in equation (2) is included, so positive values correspond to acceleration.

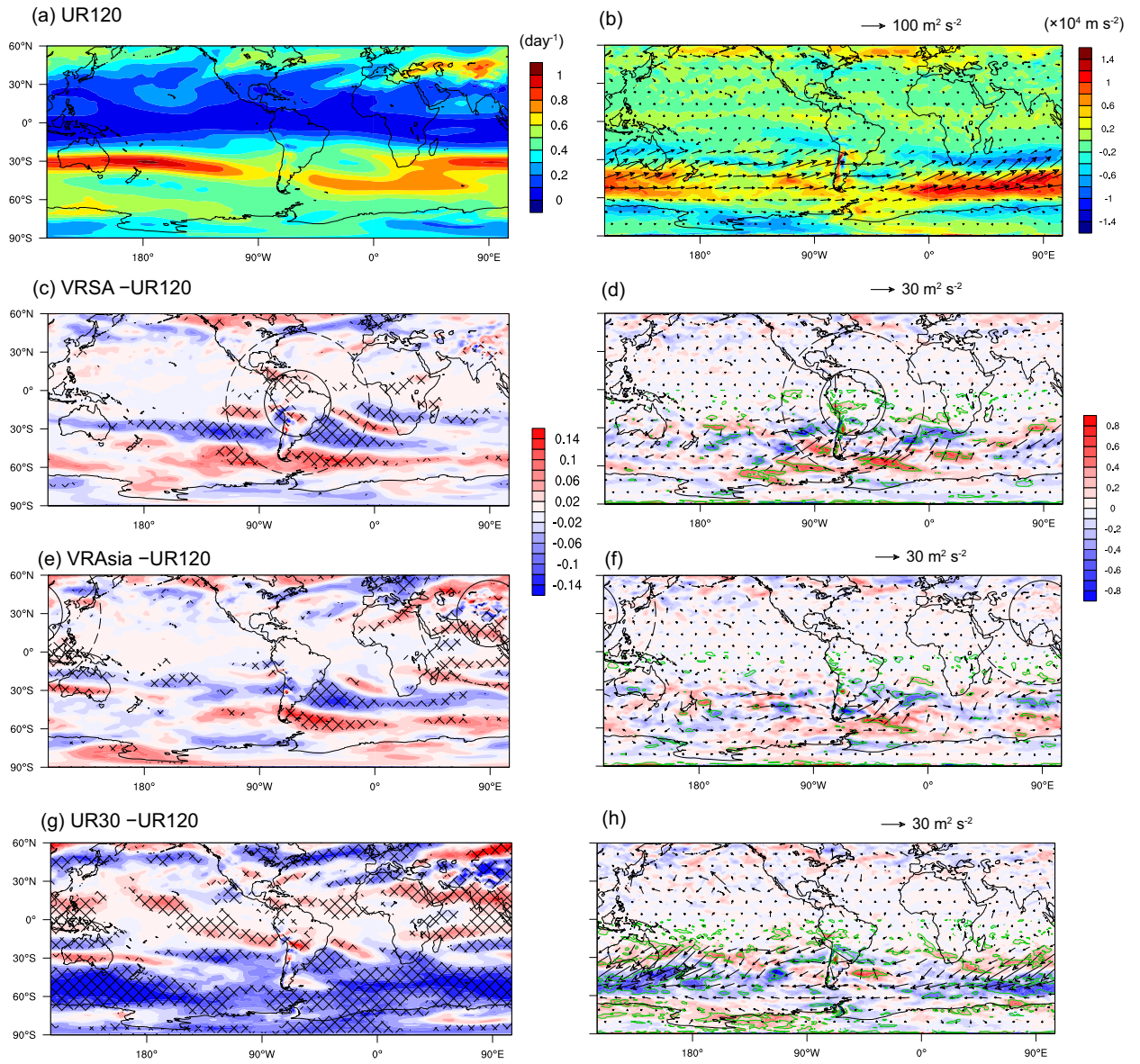

Figure 8. (left column) JJA mean Eady growth rate at the 400 hPa level, (right column) convergence of eddy zonal momentum flux (color) and W-vector (arrows) calculated from the band-pass filtered (2.5–6 days) wind at the 250 hPa level. (a and b) The results from UR120, (c and d) the differences between VRSA and UR120 (VRSA − UR120), and (e and f) for (VRAsia − UR120), (g and h) for (UR30 − UR120). The convergence of momentum flux (acceleration) is shown as positive values. Green contours in Figures 8d, 8f, and 8h depict the grid points (in the Southern Hemisphere only) with local significance at $\alpha = 0.05$ level in the difference of momentum flux convergence between each simulation and UR120.

strong SST gradient (Figure 6) and also with the westerly jet, including the two-branch structure over the South Pacific. The difference plot between VRSA and UR120 (Figure 8c) shows the poleward shift of the baroclinically unstable region over the eastern Pacific and also over the South Atlantic where we see a statistically significant anomaly of the upper level divergent flow (Figure 4d). An almost identical poleward shift over the South Atlantic is seen in the VRAsia versus UR120 comparison. This shift again can be linked to the upper level divergent circulation changes induced by the altered precipitation in the Asian Monsoon, but as will be shown, enhanced stationary Rossby wave propagation over this region in VRAsia can also alter atmospheric stability [e.g., *van der Wiel et al.*, 2015]. On the other hand, σ_{BI} in UR30 is weakened over most of the Southern Hemisphere poleward of ~30°S (Figure 8g).

The convergence of eddy momentum flux exhibits a spatial distribution similar to that of σ_{BI} (Figure 8, right column), but its maximum is slightly poleward and aligns with the eddy-driven part of the jet and the Southern Hemisphere storm track [*Trenberth*, 1991; *Nakamura and Shimpo*, 2004]. The wave activity flux is

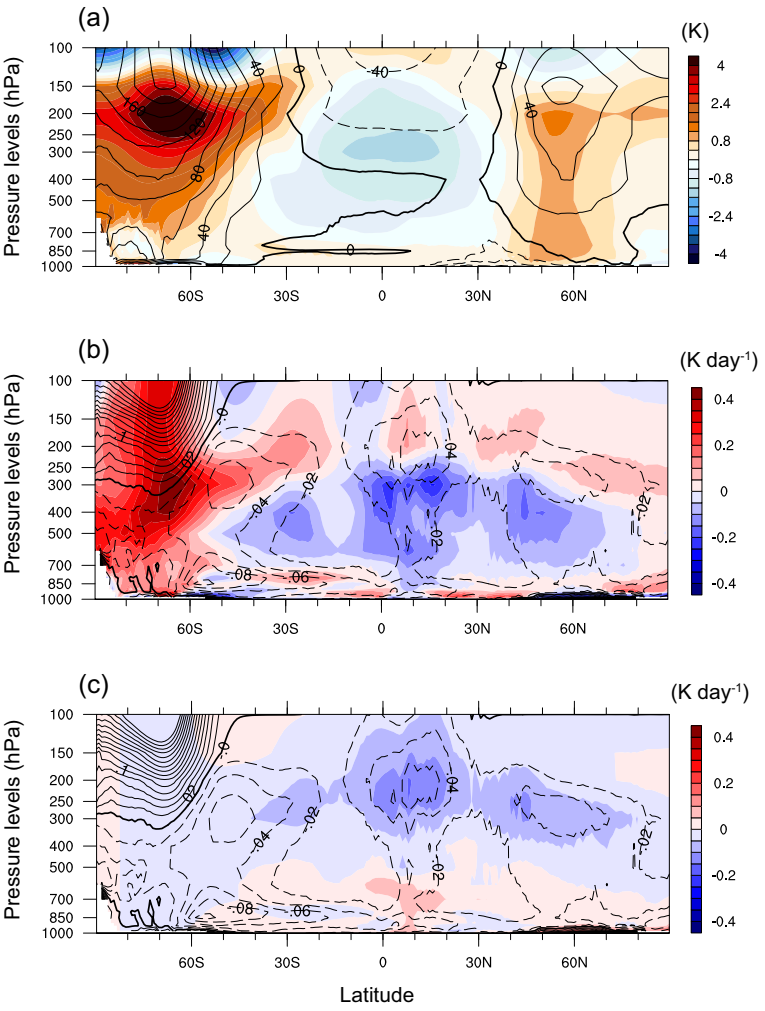

Figure 9. JJA-mean and zonal-mean profiles of thermodynamic variables illustrating the resolution sensitivity of cloud radiative forcing: (a) temperature (color, K) and geopotential height (line contour, m), (b) net radiative heating (color, K d^{-1}) and cloud fraction (line contour), and (c) net shortwave radiative heating (color, K d^{-1}) and cloud fraction (line contour). All plots represent the difference between UR30 and UR120 (UR30 minus UR120).

diagnosed using the **W** vector (section 2). The source of the wave activity is the storm track, and its sink is located on the equator side of the jet. The momentum flux traces the **W** vector backward, so the momentum source is in the subtropics and the sink is located over the storm track. The **W** vector difference between VRSA and UR120 indicates that the source/sink of wave activity flux is shifted poleward just like σ_{BI} (Figure 8d). The broad area of the momentum flux convergence inside the high-resolution and transition zone is consistent with the stronger westerly jet in Figure 2d. Equatorward, stronger divergence of the momentum flux (convergence of wave activity flux) is found, indicating a deceleration of the zonal flow, which also agrees with the pattern shown in the zonal jet response. This diagnosis provides strong evidence linking the upscale effect on the jet with the resolution-sensitivity of model precipitation in the tropical convective regions. Together with the result in the previous section, our analysis demonstrates the relationship among tropical diabatic heating, divergent circulations, and poleward shift of the baroclinically unstable region.

In concert with the σ_{BI} pattern, VRAsia shows a similar latitudinal shift in the high-frequency momentum flux convergence over the southern Atlantic and a hint of stronger wave activity flux originating from east of Australia (Figure 8f). Overall VRAsia's response in transient flow is weaker compared to that in VRSA. UR30 shows a weakening of the wave activity flux over all the longitudes (Figure 8h). This is because the background meridional temperature gradient is much weaker in UR30 than in UR120 (Figure 9a). The temperature difference reaches more than 4 K in some part of the southern high latitudes, and this warming

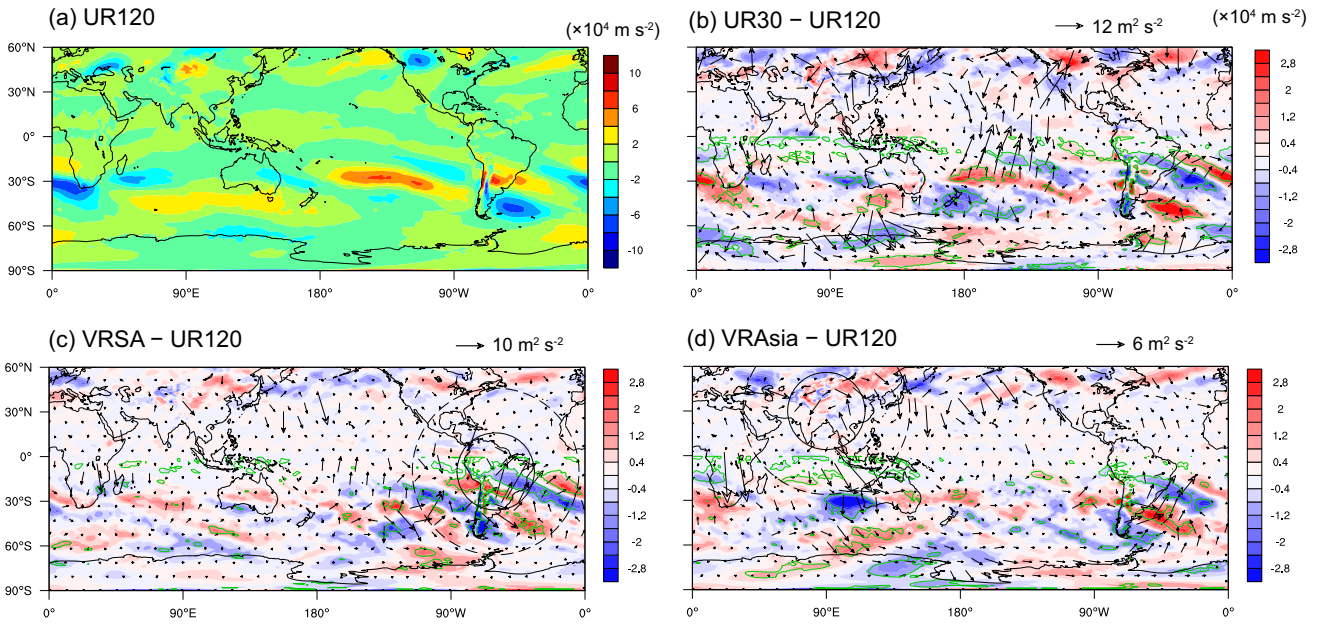

Figure 10. Convergence of eddy zonal momentum flux in the stationary component: (a) UR120, (b) UR30 minus UR120, (c) VRSA minus UR120, and (d) VRAsia minus UR120. Also shown in Figures 10b–10d is the W vector calculated based on the deviation of stream function in each simulation from that of UR120 (hence not obtained for UR120). Note the reference vector strength is different in Figures 10b–10d. The convergence of momentum flux (acceleration) is shown as positive values. Green contours in Figures 10b–10d depict the grid points (in the Southern Hemisphere only) with local significance at $\alpha = 0.05$ level in the difference of momentum flux convergence between each simulation and UR120.

pattern is well correlated with the differences in cloud fraction and radiative heating between the two simulations (Figure 9b). The dominant response in the radiative heating comes from longwave, because shortwave radiation is minimal in the winter high latitudes, and so is its difference (Figure 9c). The longwave heating maximum appears at the bottom of the cloud fraction increase in UR30 around 350 hPa and 65°S, and the warming maximum in Figure 9a is located above this heating maximum. Although our limited analysis does not explain the precise mechanism of what determines the height levels of the heating and warming maxima, the result suggests that cloud microphysics and macrophysics are the key model components behind the muted baroclinicity in UR30. It is also likely that the geographically unique aspects of Antarctica are playing a role because the cloud fraction and radiative heating in the Northern Hemisphere high latitudes are not as sensitive to resolution as in the Southern Hemisphere during the winter (not shown). The increase of the cloud cover with resolution is at odds with our general understanding of the CAM4 cloud physics, which simulated cloud cover that generally decreases with increasing resolution [*Williamson*, 2008; *Rauscher et al*., 2013; O'*Brien et al*., 2013; *Zarzycki et al*., 2014], and we are not aware of studies investigating the resolution sensitivity of the CAM4 cloud scheme over Antarctica. Changing parameters or including minor modifications in the cloud physics (e.g., as performed by *Bacmeister et al*. [2014]) may alleviate this issue, but it is beyond the scope of this work.

3.4. Stationary Waves

Strong heating from convection in the tropics can excite quasi-stationary barotropic Rossby waves that travel to the extratropics [*Trenberth et al*., 1998; *Held et al*., 2002]. For the case of the Southern Hemisphere, *Karoly et al*. [1989], *Mo and Higgins* [1998], and *Inatsu and Hoskins* [2004] presented examples of Rossby waves emanating from the tropics to the midlatitude and high latitude. Using simplified models, *Liu and Wang* [2013] and *Lee et al*. [2013] both demonstrated that barotropic stationary Rossby waves can travel from the Asian Monsoon region through the equator to affect the Southern Hemisphere circulations. Although VRSA shows an interaction between storm track and stationary waves over the eastern Pacific, here we mainly consider the possibility of waves generated or reinforced over the tropics in our VR simulations as a result of the resolution-sensitive precipitation. VRAsia clearly illustrates such a scenario.

We show in Figure 10a, the convergence of zonal momentum flux in the stationary flow at 250 hPa from UR120. An extensive convergence region appears over the subtropical South Pacific, where the tight vorticity gradient across the jet creates a narrow strip of Rossby wave source [*Ding et al*., 2012]. Another

convergence maximum occurs over northern Argentina, Uruguay, and southern Brazil (the La Plata basin), where the local maximum of precipitation takes place. The difference between UR30 and UR120 is difficult to interpret for its noisy pattern and seems to provide little useful information, except that the pattern over South America resembles that appearing in the VRSA versus UR120 and VRAsia versus UR120 comparisons as well (Figures 10b–10d). The persistence of a wave-like pattern implies a high sensitivity of the Rossby wave train over this region, which originates from both the tropics [*Ding et al*., 2012] and extratropics [*van der Wiel et al*., 2015]. Looking at VRSA versus UR120 over the eastern South Pacific in Figure 10c, the negative forcing around 30°S, 90°W and the positive forcing in its south reasonably agree with the pattern found in the upper troposphere in Figure 7d. This correspondence is indicative of the contribution of the stationary waves to the momentum budget analyzed in section 3.2, hence to the upscale effect in VRSA. The **W**-vector pattern is noisy from the eastern South Pacific to South America, and we suspect that other forcings on stationary waves are enhanced in VRSA, such as the increased precipitation over the La Plata basin [*Sakaguchi et al*., 2015] and finer topography of the Andes.

Another wave train pattern emerges in the difference between VRAsia and UR120 across the southern Indian Ocean, Southern Ocean, and Antarctica (Figure 10d, from 90°E to 180°E). The convergence/divergence pattern coincides with many features in the upper level zonal wind difference shown in Figure 2f. The **W** vector indicates that the wave activity emanates from inside the high-resolution and/or transition regions, travels southward over the Indian Ocean and Africa into the Southern Hemisphere midlatitudes, then propagates to the east along the westerly jet. Some of the wave activity further travel equatorward east of South America and break there, producing the enhanced wave-train pattern shared by VRSA and UR30. The wave sources and paths are not clear near the equator, presumably because of the quasi-geostrophic assumptions in the formulation of the **W** vector [*Takaya and Nakamura*, 2001]. But the precipitation increase in VRAsia (Figure 3f) implies wave sources from India, Southeast Asia, the South China Sea, and the Philippine Sea. Over the Indian Ocean south of the equator, we see little increase in precipitation. Thus, the apparent wave sources are mostly from the Northern Hemisphere. Here we apply the ray theory described in section 2. Using this theory, *Li et al*. [2015] demonstrated cross-equatorial wave propagations from the Northern Hemisphere to the Southern Hemisphere in the JJA climatology of a reanalysis data, particularly within the Australian-Asian monsoonal flow. Here the JJA mean zonal and meridional winds from each of UR120, UR30, and VRAsia are used as the basic states after spatial smoothing (section 2). Following *Li et al*. [2015], we consider the 300 hPa level to represent the equivalent barotropic wave motion.

The wave source region shown by the box in Figure 11 is considered first, which encloses most of the region with strong precipitation response in VRAsia and UR30 (Figure 3). The wave source points are defined every 2° in longitude and 1° in latitude for a total of 1300 points inside the rectangular region. Wave rays are integrated from all of the source points, but only rays that meet the following two conditions are examined. The first condition is based on the magnitude of Rossby wave source defined by *Sardeshmukh and Hoskins* [1988]

$$S = -\nabla \cdot \left(\mathbf{v}_\chi \zeta\right) \tag{3}$$

where v_χ is the divergent component of the wind vector and ζ is the absolute vorticity. Equation (3) is evaluated at each sample point based on the JJA climatology of wind and vorticity, and if S is less than 0.5 (10^{-10} s^{-2}) for a given point, then the wave ray from that source location is not considered. The threshold of 0.5 is rather arbitrary and represents a typical value of an interannual standard deviation of S over the oceanic regions inside the search domain (black box). The second condition is that the ray reaches the Southern Hemisphere midlatitudes (45°S) before it ends. We also need to provide the initial zonal wave number (k_0) to initiate the ray tracing, and the zonal wave number 5 is chosen in Figure 11, roughly corresponding to the zonal scale of the precipitation response (i.e., continuous positive anomaly in Figure 3f as the half wavelength). We have calculated the ray paths with k_0 from 1 to 8, and in general the cross-equatorial propagations from the above source region, are more ubiquitous with smaller k_0 and become more sparse with k_0 greater than 5.

Given the above conditions, the JJA mean state of UR120 supports little propagation of Rossby waves excited in the Northern Hemisphere to reach the Southern Hemisphere midlatitudes (Figure 11a). With the same k_0 and sampling area for the wave source, VRAsia provides far greater chances for Rossby waves to reach the Southern Hemisphere midlatitude and high latitude (Figure 11b). The evolution of the total wave

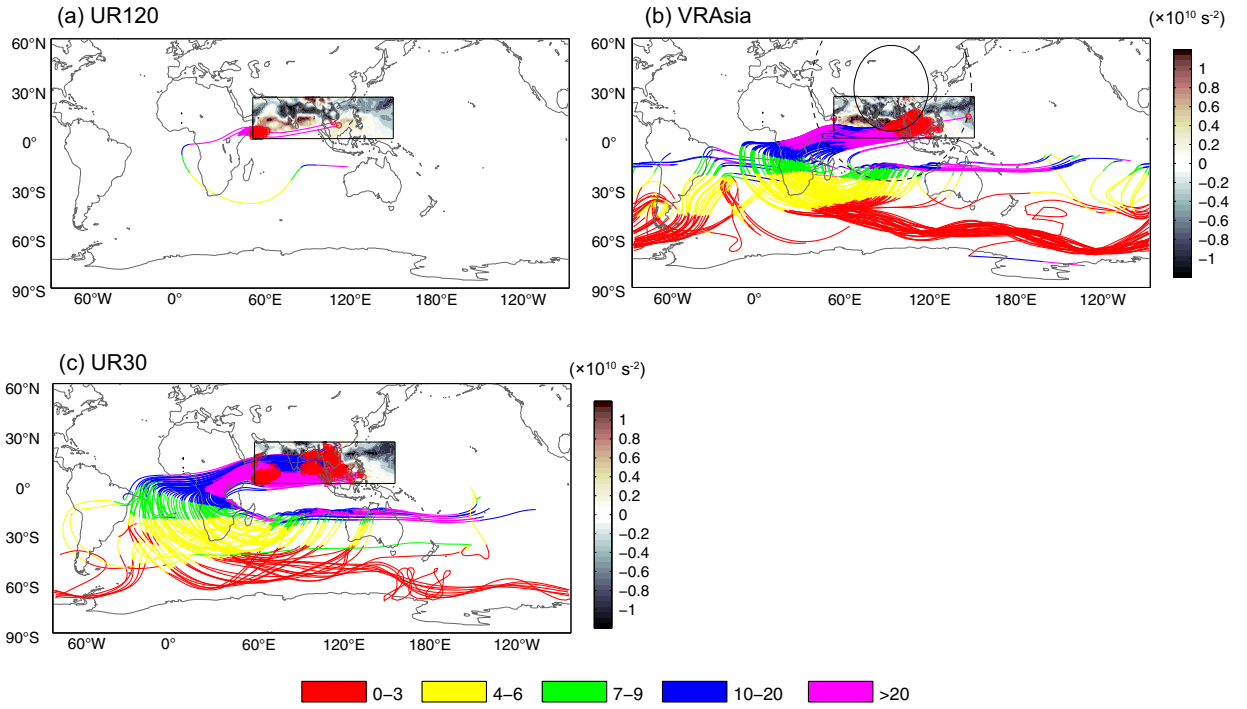

Figure 11. Ray paths of stationary Rossby waves propagating in the smoothed JJA mean wind field at the 300 hPa level: (a) UR120, (b) VRAsia, and (c) UR30. Color shading inside the rectangular box represents the wave source strength (s^{-2}) from equation (3). The colors of each ray represent the total wave number at each time step (1 h) of ray tracing. The initial zonal wave number is 5 for all the plots. See the text for details.

number (line color) for the rays crossing the equator is similar to that in *Li et al.* [2015] based on a reanalysis data. Many rays in VRAsia travel first westward from Asia and across the equator over Africa, and then propagating eastward and finally northward near South America. The ray paths over the midlatitude and high-latitude agree fairly well with the **W** vector pattern (Figure 10d), while near the tropics the latter is not able to describe the wave activity flux (e.g., the initial westward propagation from Asia) due to its quasi-geostrophic assumption. We also note that the ray tracing and the **W** vector do not completely agree on the wave activity propagating just west of Australia (discussed below). Nonetheless both diagnoses strongly suggest the influence of the heating change in the Asian monsoon region on the westerly jet over South America, via stationary waves traveling across the equator and then the Eastern and Western Hemispheres. Interestingly, UR30 also exhibits much higher potential of cross-equatorial propagations, with propagation paths quite similar to those found in VRAsia (Figure 11c). It is not expected that the details of the ray trajectories from UR30 and VRAsia would agree with each other because of the difference in the background circulations in the coarse-resolution domain.

Examining UR120 and VRAsia in more detail, their difference comes partly from *S* (equation (3)) being stronger in VRAsia. But the basic state wind field in VRAsia is also more favorable for the waves to reach the Southern Hemisphere midlatitudes. In Figure 12a, the rays from the source locations in the VRAsia case (those in Figure 11b) are traced in the UR120 basic state. Compared to Figure 11a, we see many more waves traveling across the easterly regions over Africa, but most of them are refracted and then break at the equator side of the westerly jet over the Indian Ocean and Australia. Figure 12b shows the wave propagations from the wave source in UR120 (as in Figure 11a) but in the VRAsia's basic state. In this case, wave propagations are sparse and similar to that in UR120. Still, the sharp contrast between Figure 11b and Figure 12a delineates the importance of the basic state flow, which is likely related back to the influence of precipitation on the monsoonal circulation. The cross-equatorial wave propagation strongly depends on the northerly meridional flow [*Lee et al.*, 2013; *Liu and Wang*, 2013; *Li et al.*, 2015], and the northerly flow is indeed enhanced in VRAsia compared to UR120 (the divergent wind in Figure 4f and also in the rotational wind, not shown).

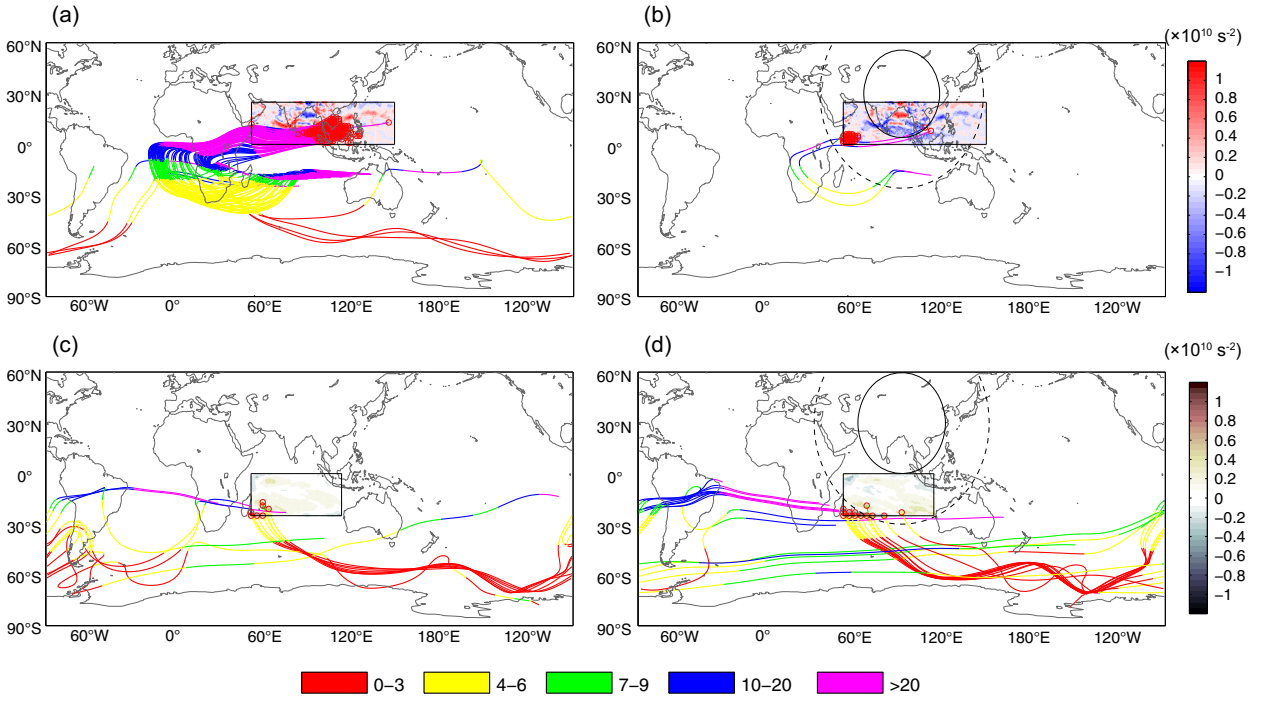

Figure 12. Sensitivity of ray tracing (top) to swapping the wave sources and background flows and (bottom) to different wave source locations. In the top row: (a) the Rossby wave rays from the wave sources identified for VRAsia (as in Figure 11b) but traced in the UR120 basic flow, (b) the rays from the wave sources identified for UR120 (as in Figure 11a) but traced in the VRAsia basic flow. The color shading in Figures 12a and 12b indicates the difference in the wave source strength between VRAsia and UR120. In the bottom row: (c) the ray paths in UR120 from the wave sources in the southern Indian Ocean; (d) the ray paths in VRAsia from the southern Indian Ocean. The color shading in Figures 12c and 12d represents the wave source strength in UR120 and VRAsia (not the difference), respectively. The initial zonal wave number is 5 in Figures 12a and 12b and 3 in Figures 12c and 12d.

Finally, a few remarks are in order regarding the wave activity flux and momentum flux convergence over the eastern Indian Ocean (25°S–60°S, 95°E–130°E). Even though the overall impact of the aforementioned flux convergence on the upper level jet may not be significant around the west of Australia according to Figure 2f, the robustness of their signals in Figure 10 and their absence in the ray tracing (Figure 11b) warrant an explanation. The absence of such rays is partly due to the spatial smoothing we applied to the basic state for ray tracing, which tends to enhance the zonal wind rather than the meridional wind (e.g., the easterly over Indonesia; supporting information Figure S4). We also note two other possibilities. First, we see more rays across the eastern Indian Ocean when we extend the source region to the east around the dateline (not shown, but see *Li et al.* [2015, Figure 11a]). Stronger wave activity over there in VRAsia is possible because the upper level divergence anomaly spreads to the east near the dateline (Figure 4f), and there are some hints of stronger wave activity flux in the subtropics over the northern central Pacific (∼30°N, 150°E–180°E, Figure 10d). Another possibility is that the wave originates in the Indian Ocean. *Sardeshmukh and Hoskins* [1988] proposed that a wave source can be created by vorticity advection by the divergent circulation due to convection, so divergent sources in the Northern Hemisphere can induce wave sources in the Southern Hemisphere. Equation (3) includes this process as well. S is much weaker over the Indian Ocean compared to the Asian monsoon region, but values greater than 0.4 are still common. Using 0.4 for the wave source threshold and the initial zonal wave number 3, we see some Rossby waves traveling over the eastern Indian Ocean to the midlatitudes, particularly in VRAsia (Figures 12c and 12d). In any case, the above diagnoses strongly suggest that perturbations associated with the heating anomaly of 15–20% in the Asian Monsoon, regardless of their physical or artificial origins, can propagate from the Northern Hemisphere across the equator to produce discernable impacts on the large-scale circulation in the Southern Hemisphere midlatitudes.

4. Discussion

Our previous study showed that in the AMIP case, MPAS-CAM4 VR reproduces the behavior of the quasi-uniform high-resolution simulation inside the high-resolution domain [*Sakaguchi et al.*, 2015]. We are

interested if this is also true for the upscale effects. If the same upscale effect is found in both VR and quasi-uniform high-resolution simulations, then we consider the upscale effect as "consistent" because VR reproduces scale interactions that occur in the reference high-resolution simulation. Conversely, an upscale effect is inconsistent if its sources and/or pathways are unique to the VR simulation. From this point of view, the upscale effect found by *Rauscher et al*. [2013] and *Hagos et al*. [2013] in the aquaplanet case is inconsistent because the anomalous precipitation and heating appeared mainly on the *downwind side* of the refined domain, so the prominent Rossby wave response to the heating in VR cannot be found in the reference high-resolution simulation, which is zonally symmetric.

In AMIP simulations, based on the result in section 3.4, the stationary Rossby wave from the Asian Monsoon region seems to be a consistent upscale effect. The increase in the number of possible cross-equatorial ray paths and their spatial patterns are generally consistent between UR30 and VRAsia when compared to UR120 (Figures 11b and 11c). The implication is that when a reference high-resolution simulation is able to improve regional features relative to a coarse-resolution simulation, particularly those with regional and global impacts as extensive as the Asian Monsoon, then MPAS-VR is not only able to reproduce the improvement inside the high-resolution domain, but it also upscales the improved local processes to large-scale circulations in a manner consistent with the reference high-resolution simulation (e.g., Rossby wave teleconnection). As for the origin of the resolution sensitivity of the Asian Monsoon precipitation in this study, test simulations of VRAsia with coarse-resolution topography (using a less expensive $\times 8$ refinement from 240 to 30 km grid, not shown) suggest that most of the changes come from the resolution sensitivity of the physics parameterizations rather than the more finely resolved topography and other land surface characteristics. Therefore, proper scale-awareness of the moist parameterizations seems crucial for local improvement in the Asian Monsoon and the associated consistent, desirable upscale effects.

No conclusion can be drawn from the result of this study (section 3.3) on the consistency of the upscale effect associated with the poleward shift of the baroclinically unstable region around South America, the origin of which is traced back to the enhanced condensational heating in the tropics via expanded upper level divergent circulations. The baroclinic instability across the whole Southern Hemisphere extratropics in UR30 is weakened compared to UR120 as a result of changes in cloud fraction and its impact on radiative heating, which are artifacts of resolution sensitivity. The signal from this radiative heating is so dominant that the effects of other regional forcings in the VR simulations cannot be detected. However, it is important to confirm the consistency of this pathway of upscale effect because the resolution sensitivity of synoptic wave disturbances and westerly jet can affect the advection of scalars, such as aerosols [*Ma et al*., 2014] and water vapor along atmospheric rivers [*Hagos et al*., 2015]. The implication is that VR simulations may potentially improve modeling of extreme hydrological events and aerosol effects through the local impacts of resolution on wave activity or remote impacts through changes in wave propagations. It is also possible that the poleward shift of the jet is contributed from the resolution dependence of the *propagation and dissipation* of wave activity [*Lu et al*., 2015], not only from the poleward shift of its *source* as shown in our comparison between UR120 and the VR simulations. The former attribution is yet to be investigated because the diagnosis method used in *Lu et al*. [2015] is based on a zonal mean budget and thus not directly applicable to a zonally nonuniform grid refinement. Future work using a recently developed framework of local wave activity [*Huang and Nakamura*, 2016] and models with more physical resolution sensitivity of cloud fraction over Antarctica may further elucidate the dynamical linkages between the midlatitude wave activity and upscale effect on the jet.

5. Conclusions

A previous study [*Sakaguchi et al*., 2015] evaluated the VR simulations of the MPAS-A dynamical core coupled to the CAM4 physics parameterizations and identified changes in the large-scale circulations, the so-called upscale effects, both locally in and remotely away from the region of refinement. The strongest upscale effect was detected in the Southern Hemisphere jets during the austral winter (June-July-August). This study presents a more detailed diagnosis to identify the physical and dynamical processes behind the particular upscale effect on the Southern Hemisphere jet.

In three VR simulations with regional refinements over North America, South America, and Asia, we find links between the westerly jet in the Southern Hemisphere and the increased precipitation inside the high-

resolution regions and/or transition zones, particularly in regions dominated by convective precipitation such as the ITCZ and the Asian monsoon region. One pathway for the upscale effects can be the divergent circulation from the tropics, for instance the local Hadley cell, which is meridionally expanded by the stronger heating in the high-resolution region over the tropics. As the descending branch of the Hadley cell is shifted poleward, so are the regions of strong baroclinic instability and the momentum flux convergence associated with the baroclinic Rossby waves. Another pathway found in this study is stationary Rossby waves propagating across the equator from the Northern Hemisphere. In particular, the upscale effect through the enhanced stationary Rossby waves from the Asian Monsoon region is generally consistent with the simulation using the quasi-uniform high-resolution grid (UR30). The implication is that if one can improve model precipitation in the Asian Monsoon by increasing resolution, then MPAS-VR is able to improve not only the simulation inside the high-resolution domain locally, but also to upscale the local gain in skill to the Southern Hemisphere and produce a desirable impact on the large-scale circulations. This result emphasizes the importance for similar analyses to be performed with other global VR frameworks to facilitate interpretations of modeling experiments using the VR modeling approach.

Acknowledgments

All data and simulation output used in this study are archived at the National Energy Research Scientific Computing Center (NERSC) and can be accessed by contacting L. Ruby Leung (ruby.leung@pnnl.gov). The authors thank the anonymous reviewers for their valuable comments and Bryce Harrop for helpful discussions. This study was supported by the U.S. Department of Energy (DOE) Office of Science Biological and Environmental Research as part of the Regional and Global Climate Modeling program. The contribution of Y. Li was supported by grant 41575060 from the National Natural Science Foundation of China. This research used computational resources from the National Energy Research Scientific Computing Center (NERSC), a DOE User Facility supported by the Office of Science under contract DE-AC02-05CH11231. Additional computational resources were provided by the Pacific Northwest National Laboratory (PNNL) Institutional Computing program. PNNL is operated for DOE by Battelle Memorial Institute under contract DE-AC05-76RL01830.

References

Ambrizzi, T., B. J. Hoskins, and H.-H. Hsu (1995), Rossby wave propagation and teleconnection patterns in the austral winter, *J. Atmos. Sci.*, *52*(21), 3661–3672, doi:10.1175/1520-0469(1995)052 < 3661:RWPATP>2.0.CO;2.

Arakawa, A., J.-H. Jung, and C.-M. Wu (2011), Toward unification of the multiscale modeling of the atmosphere, *Atmos. Chem. Phys.*, *11*(8), 3731–3742, doi:10.5194/acp-11-3731-2011.

Arakelian, A., and F. Codron (2012), Southern Hemisphere jet variability in the IPSL GCM at varying resolutions, *J. Atmos. Sci.*, *69*, 3788–3799, doi:10.1175/JAS-D-12-0119.1.

Bacmeister, J. T., M. F. Wehner, R. B. Neale, A. Gettelman, C. Hannay, P. H. Lauritzen, J. M. Caron, and J. E. Truesdale (2014), Exploratory high-resolution climate simulations using the Community Atmosphere Model (CAM), *J. Clim.*, *27*(9), 3073–3099, doi:10.1175/JCLI-D-13-00387.1.

Bals-Elsholz, T. M., E. H. Atallah, L. F. Bosart, T. A. Wasula, M. J. Cempa, and A. R. Lupo (2001), The wintertime southern hemisphere split jet: Structure, variability, and evolution, *J. Clim.*, *14*, 4191–4215.

Bühler, O. (2009), *Waves and Mean Flows*, 1st ed., Cambridge Univ. Press, N. Y.

Chen, W., Z. Jiang, L. Li, and P. Yiou (2011), Simulation of regional climate change under the IPCC A2 scenario in southeast China, *Clim. Dyn.*, *36*, 491–507, doi:10.1007/s00382-010-0910-3.

Dee, D. P., et al. (2011), The ERA-Interim reanalysis: Configuration and performance of the data assimilation system, *Q. J. R. Meteorol. Soc.*, *137*, 553–597, doi:10.1002/qj.828.

Ding, Q., E. J. Steig, D. S. Battisti, and J. M. Wallace (2012), Influence of the tropics on the Southern Annular Mode, *J. Clim.*, *25*(18), 6330–6348, doi:10.1175/JCLI-D-11-00523.1.

Farrell, B., and I. Watterson (1985), Rossby waves in opposing currents, *J. Atmos. Sci.*, *42*(16), 1746–1756.

Flato, G., et al. (2013), Evaluation of Climate Models, in *Climate Change 2013: The Physical Science Basis. Contribution of Working Group I to the Fifth Assessment Report of the Intergovernmental Panel on Climate Change*, edited by T. F. Stocker et al., pp. 741–866, Cambridge Univ. Press, Cambridge, U. K.

Godfrey, J. S., and S. R. Rintoul (1998), The role of the oceans in Southern Hemisphere climate, in *Meteorology of the Southern Hemisphere*, edited by D. J. Karoly and D. G. Vincent, pp. 283–306, Am. Meteorol. Soc., Boston, Mass.

Hagos, S., L. R. Leung, S. A. Rauscher, and T. Ringler (2013), Error characteristics of two grid refinement approaches in aquaplanet simulations: MPAS-A and WRF, *Mon. Weather Rev.*, *141*(9), 3022–3036, doi:10.1175/MWR-D-12-00338.1.

Hagos, S., L. R. Leung, Q. Yang, C. Zhao, and J. Lu (2015), Resolution and dynamical core dependence of atmospheric river frequency in global model simulations, *J. Clim.*, *28*(7), 2764–2776, doi:10.1175/JCLI-D-14-00567.1.

Harris, L. M., and S.-J. Lin (2013), A two-way nested global-regional dynamical core on the cubed-sphere grid, *Mon. Weather Rev.*, *141*(1), 283–306, doi:10.1175/MWR-D-11-00201.1.

Harris, L. M., and S.-J. Lin (2014), Global-to-regional nested grid climate simulations in the GFDL high resolution atmospheric model, *J. Clim.*, *27*, 4890–4910, doi:10.1175/JCLI-D-13-00596.1.

Held, I. M., and B. J. Hoskins (1985), Large-scale eddies and the general circulation of the troposphere, *Adv. Geophys.*, *28A*, 3–31.

Held, I. M., M. Ting, and H. Wang (2002), Northern winter stationary waves: Theory and modeling, *J. Clim.*, *15*, 2125–2144.

Hirota, N., and M. Takahashi (2012), A tripolar pattern as an internal mode of the East Asian summer monsoon, *Clim. Dyn.*, *39*(9-10), 2219–2238, doi:10.1007/s00382-012-1416-y.

Hoskins, B. J., and D. J. Karoly (1981), The steady linear response of a spherical atmosphere to thermal and orographic forcing, *J. Atmos. Sci.*, *38*, 1179–1196.

Hoskins, B. J., and P. J. Valdes (1990), On the existence of storm-tracks, *J. Atmos. Sci.*, *47*(15), 1854–1864.

Hoskins, B. J., and B. Wang (2006), Large-scale atmospheric dynamics, in *The Asian Monsoon*, edited by B. Wang, pp. 357–406, Springer, N. Y.

Huang, C. S.-Y., and N. Nakamura (2016), Local finite-amplitude wave activity as a diagnostic of anomalous weather events, *J. Atmos. Sci.*, *73*, 211–229, doi:10.1175/JAS-D-15-0194.1.

Huffman, G. J., R. F. Adler, D. T. Bolvin, and G. Gu (2009), Improving the global precipitation record: GPCP version 2.1, *Geophys. Res. Lett.*, *36*, L17808, doi:10.1029/2009GL040000.

Hurrell, J. W., J. J. Hack, D. Shea, J. M. Caron, and J. Rosinski (2008), A new sea surface temperature and sea ice boundary dataset for the Community Atmosphere Model, *J. Clim.*, *21*(19), 5145–5153, doi:10.1175/2008JCLI2292.1.

Inatsu, M., and B. J. Hoskins (2004), The zonal asymmetry of the Southern Hemisphere winter storm track, *J. Clim.*, *17*, 4882–4892.

Inatsu, M., Y. Satake, M. Kimoto, and N. Yasutomi (2012), GCM bias of the western Pacific summer monsoon and its correction by two-way nesting system, *J. Meteorol. Soc. Jpn.*, *90B*(2003), 1–10, doi:10.2151/jmsj.2012-B01.

Ju, L., T. Ringler, and M. Gunzburger (2011), Voronoi tessellations and their application to climate and global modeling, in *Numerical Techniques for Global Atmospheric Models*, vol. 80, edited by P. Lauritzen et al., pp. 313–342, Springer, Berlin.
Karoly, D. J., R. A. Plumb, and M. Ting (1989), Examples of the horizontal propagation of quasi-stationary waves, *J. Atmos. Sci.*, *46*(18), 2802–2811.
Karoly, D. J., D. G. Vincent, and J. M. Schrage (1998), General circulation, in *Meteorology of the Southern Hemisphere*, edited by D. J. Karoly and D. G. Vincent, pp. 47–85, Am. Meteorol. Soc., Boston, Mass.
Lawrence, D. M., et al. (2011), Parameterization improvements and functional and structural advances in version 4 of the Community Land Model, *J. Adv. Model. Earth Syst.*, *3*, M03001, doi:10.1029/2011MS000045.
Lee, S.-K., C. R. Mechoso, C. Wang, and J. D. Neelin (2013), Interhemispheric influence of the northern summer monsoons on southern subtropical anticyclones, *J. Clim.*, *26*(24), 10,193–10,204, doi:10.1175/JCLI-D-13-00106.1.
Leung, L. R., T. D. Ringler, W. D. Collins, M. A. Taylor, and M. Ashfaq (2013), A hierarchical evaluation of regional climate simulations, *Eos Trans. AGU*, *94*(34), 297–298, doi:10.1002/2013EO340001.
Li, Y., J. Li, F. F. Jin, and S. Zhao (2015), Interhemispheric propagation of stationary Rossby waves in the horizontally nonuniform background flow, *J. Atmos. Sci.*, *72*, 3233–3256, doi:10.1175/JAS-D-14-0239.1.
Lindzen, R. S., and B. Farrell (1980), A simple approximate result for the maximum growth rate of baroclinic instabilities, *J. Atmos. Sci.*, *37*, 1648–1654.
Liu, F., and B. Wang (2013), Mechanisms of global teleconnections associated with the Asian summer monsoon: An intermediate model analysis, *J. Clim.*, *26*, 1791–1806, doi:10.1175/JCLI-D-12-00243.1.
Lorenz, P., and D. Jacob (2005), Influence of regional scale information on the global circulation: A two-way nesting climate simulation, *Geophys. Res. Lett.*, *32*, L18706, doi:10.1029/2005GL023351.
Lu, J., G. Chen, L. R. Leung, D. A. Burrows, Q. Yang, K. Sakaguchi, and S. Hagos (2015), Towards the dynamical convergence on the jet stream in aquaplanet AGCMs, *J. Clim.*, *28*, 6763–6782, doi:10.1175/JCLI-D-14-00761.1.
Ma, P. L., P. J. Rasch, J. D. Fast, R. C. Easter, W. I. Gustafson, X. Liu, S. J. Ghan, and B. Singh (2014), Assessing the CAM5 physics suite in the WRF-Chem model: Implementation, resolution sensitivity, and a first evaluation for a regional case study, *Geosci. Model Dev.*, *7*, 755–778, doi:10.5194/gmd-7-755-2014.
Martini, M. N., W. I. Gustafson, T. A. O'Brien, and P. L. Ma (2015), Evaluation of tropical channel refinement using MPAS-A aquaplanet simulations, *J. Adv. Model. Earth Syst.*, *7*, 1351–1367, doi:10.1002/2015MS000470.
Medvigy, D., R. L. Walko, and R. Avissar (2011), Effects of deforestation on spatiotemporal distributions of precipitation in South America, *J. Clim.*, *24*(8), 2147–2163, doi:10.1175/2010JCLI3882.1.
Medvigy, D., R. L. Walko, M. J. Otte, and R. Avissar (2013), Simulated changes in northwest U.S. climate in response to Amazon deforestation, *J. Clim.*, *26*(22), 9115–9136, doi:10.1175/JCLI-D-12-00775.1.
Mo, K. C., and R. W. Higgins (1998), The Pacific–South American modes and tropical convection during the Southern Hemisphere winter, *Mon. Weather Rev.*, *126*, 1581–1596.
Nakamura, H., and A. Shimpo (2004), Seasonal variations in the Southern Hemisphere storm tracks and jet streams as revealed in a reanalysis dataset, *J. Clim.*, *17*(9), 1828–1844.
Neale, R. B., and B. J. Hoskins (2001), A standard test for AGCMs including their physical parameterizations: I: The proposal, *Atmos. Sci. Lett.*, *1*(2), 108–114, doi:10.1006/asle.2000.0020.
Neale, R. B., et al. (2010), Description of the NCAR Community Atmosphere Model (CAM 4.0), *NCAR Tech. Note NCAR/TN-485+STR*, 194 pp., National Center for Atmospheric Research (NCAR), Boulder, Colo.
O'Brien, T. A., F. Li, W. D. Collins, S. A. Rauscher, T. D. Ringler, M. Taylor, S. M. Hagos, and L. R. Leung (2013), Observed scaling in clouds and precipitation and scale incognizance in regional to global atmospheric models, *J. Clim.*, *26*(23), 9313–9333, doi:10.1175/JCLI-D-13-00005.1.
Park, S.-H., W. C. Skamarock, J. B. Klemp, L. D. Fowler, and M. G. Duda (2013), Evaluation of global atmospheric solvers using extensions of the Jablonowski and Williamson baroclinic wave test case, *Mon. Weather Rev.*, *141*(9), 3116–3129, doi:10.1175/MWR-D-12-00096.1.
Park, S.-H., J. B. Klemp, and W. C. Skamarock (2014), A comparison of mesh refinement in the global MPAS-A and WRF models using an idealized normal-mode baroclinic wave simulation, *Mon. Weather Rev.*, *142*, 3614–3634, doi:10.1175/MWR-D-14-00004.1.
Pielke, R. A. S. (1991), A recommended specific definition of "Resolution," *Bull. Am. Meteorol. Soc.*, *72*(12), 1914.
Pope, V. D., and R. A. Stratton (2002), The processes governing horizontal resolution sensitivity in a climate model, *Clim. Dyn.*, *19*(3-4), 211–236, doi:10.1007/s00382-001-0222-8.
Rauscher, S. A., and T. D. Ringler (2014), Impact of variable-resolution meshes on midlatitude baroclinic eddies using CAM-MPAS-A, *Mon. Weather Rev.*, *142*(11), 4256–4268, doi:10.1175/MWR-D-13-00366.1.
Rauscher, S. A., T. D. Ringler, W. C. Skamarock, and A. A. Mirin (2013), Exploring a global multiresolution modeling approach using aquaplanet simulations, *J. Clim.*, *26*(8), 2432–2452, doi:10.1175/JCLI-D-12-00154.1.
Richter, J. H., and P. J. Rasch (2008), Effects of convective momentum transport on the atmospheric circulation in the Community Atmosphere Model, version 3, *J. Clim.*, *21*(7), 1487–1499, doi:10.1175/2007JCLI1789.1.
Ringler, T. D., L. Ju, and M. Gunzburger (2008), A multiresolution method for climate system modeling: Application of spherical centroidal Voronoi tessellations, *Ocean Dyn.*, *58*(5-6), 475–498, doi:10.1007/s10236-008-0157-2.
Ringler, T. D., D. Jacobsen, M. Gunzburger, L. Ju, M. Duda, and W. C. Skamarock (2011), Exploring a multiresolution modeling approach within the shallow-water equations, *Mon. Weather Rev.*, *139*(11), 3348–3368, doi:10.1175/MWR-D-10-05049.1.
Sakaguchi, K., L. R. Leung, C. Zhao, Q. Yang, J. Lu, S. Hagos, S. A. Rauscher, L. Dong, T. D. Ringler, and P. H. Lauritzen (2015), Exploring a multiresolution approach using AMIP simulations, *J. Clim.*, *28*(14), 5549–5574, doi:10.1175/JCLI-D-14-00729.1.
Sardeshmukh, P. D., and B. J. Hoskins (1988), The generation of global rotational flow by steady idealized tropical divergence, *J. Atmos. Sci.*, *45*(7), 1228–1251.
Schneider, E. K., and I. G. Watterson (1984), Stationary Rossby wave propagation through easterly layers, *J. Atmos. Sci.*, *41*(13), 2069–2083.
Simpson, I. R., T. A. Shaw, and R. Seager (2014), A diagnosis of the seasonally and longitudinally varying midlatitude circulation response to global warming, *J. Atmos. Sci.*, *71*, 2489–2515, doi:10.1175/JAS-D-13-0325.1.
Skamarock, W. C. (2004), Evaluating mesoscale NWP models using kinetic energy spectra, *Mon. Weather Rev.*, *132*(12), 3019–3032, doi:10.1175/MWR2830.1.
Skamarock, W. C., J. B. Klemp, J. Dudhia, D. O. Gill, D. M. Barker, M. G. Duda, X.-Y. Huang, W. Wang, and J. G. Powers (2008), A description of the advanced research WRF version 3, *NCAR Tech. Note NCAR/TN–475+STR*, 113 pp., National Center for Atmospheric Research (NCAR), Boulder, Colo.
Skamarock, W. C., J. B. Klemp, M. G. Duda, L. D. Fowler, S.-H. Park, and T. D. Ringler (2012), A multiscale nonhydrostatic atmospheric model using Centroidal Voronoi Tesselations and C-grid staggering, *Mon. Weather Rev.*, *140*(9), 3090–3105, doi:10.1175/MWR-D-11-00215.1.

Takaya, K., and H. Nakamura (2001), A formulation of a phase-independent wave-activity flux for stationary and migratory quasigeostrophic eddies on a zonally varying basic flow, *J. Atmos. Sci.*, *58*, 608–627.
Taylor, M. A., and A. Fournier (2010), A compatible and conservative spectral element method on unstructured grids, *J. Comput. Phys.*, *229*(17), 5879–5895, doi:10.1016/j.jcp.2010.04.008.
Trenberth, K. E. (1986), An assessment of the impact of transient eddies on the zonal flow during a blocking episode using localized Eliassen-Palm flux diagnostics, *J. Atmos. Sci.*, *43*(19), 2070–2087.
Trenberth, K. E. (1991), Storm tracks in the Southern Hemisphere, *J. Atmos. Sci.*, *48*(19), 2159–2178.
Trenberth, K. E., G. W. Branstator, D. Karoly, A. Kumar, N.-C. Lau, and C. Ropelewski (1998), Progress during TOGA in understanding and modeling global teleconnections associated with tropical sea surface temperatures, *J. Geophys. Res.*, *103*(C7), 14,291–14,324, doi:10.1029/97JC01444.
Trenberth, K. E., J. W. Hurrell, and D. P. Stepaniak (2006), The Asian monsoon: Global perspectives, in *The Asian Monsoon*, edited by B. Wang, pp. 67–87, Springer, N. Y.
Vallis, G. K. (2006), *Atmospheric and Oceanic Fluid Dynamics*, 1st ed., Cambridge Univ. Press, N. Y.
van der Wiel, K., A. J. Matthews, D. P. Stevens, and M. M. Joshi (2015), A dynamical framework for the origin of the diagonal South Pacific and South Atlantic Convergence Zones, *Q. J. R. Meteorol. Soc.*, *141*, 1997–2010, doi:10.1002/qj.2508.
Ventura, V., C. J. Paciorek, and J. S. Risbey (2004), Controlling the proportion of falsely rejected hypotheses when conducting multiple tests with climatological data, *J. Clim.*, *17*, 4343–4356.
Vincent, D. G. (1994), The South Pacific convergence zone (SPCZ): A review, *Mon. Weather Rev.*, *122*(9), 1949–1970.
Walko, R. L., and R. Avissar (2011), A direct method for constructing refined regions in unstructured conforming triangular–hexagonal computational grids: Application to OLAM, *Mon. Weather Rev.*, *139*(12), 3923–3937, doi:10.1175/MWR-D-11-00021.1.
Wan, H., M. A. Giorgetta, and L. Bonaventura (2008), Ensemble Held–Suarez test with a spectral transform model: Variability, sensitivity, and convergence, *Mon. Weather Rev.*, *136*(3), 1075–1092, doi:10.1175/2007MWR2044.1.
Wang, S.-Y., L. Hipps, R. R. Gillies, and J.-H. Yoon (2014), Probable causes of the abnormal ridge accompanying the 2013–2014 California drought: ENSO precursor and anthropogenic warming footprint, *Geophys. Res. Lett.*, *41*, 799–804, doi:10.1002/2013GL058954.
Watterson, I. G., and E. K. Schneider (1987), The effect of the Hadley circulation on the meridional propagation of stationary waves, *Q. J. R. Meteorol. Soc.*, *113*, 779–813.
Wilks, D. S. (2006), On "Field Significance" and the False Discovery Rate, *J. Appl. Meteorol. Climatol.*, *45*(9), 1181–1189, doi:10.1175/JAM2404.1.
Williamson, D. L. (2008), Convergence of aqua-planet simulations with increasing resolution in the Community Atmospheric Model, version 3, *Tellus, Ser. A*, *60*(5), 848–862, doi:10.1111/j.1600-0870.2008.00339.x.
Zarzycki, C. M., and C. Jablonowski (2014), A multidecadal simulation of Atlantic tropical cyclones using a variable-resolution global atmospheric general circulation model, *J. Adv. Model. Earth Syst.*, *6*, 1–24, doi:10.1002/2014MS000352.
Zarzycki, C. M., M. N. Levy, C. Jablonowski, J. R. Overfelt, M. A. Taylor, and P. A. Ullrich (2014), Aquaplanet experiments using CAM's variable-resolution dynamical core, *J. Clim.*, *27*(14), 5481–5503, doi:10.1175/JCLI-D-14-00004.1.
Zarzycki, C. M., C. Jablonowski, D. R. Thatcher, and M. A. Taylor (2015), Effects of localized grid refinement on the general circulation and climatology in the Community Atmosphere Model, *J. Clim.*, *28*(7), 2777–2803, doi:10.1175/JCLI-D-14-00599.1.
Zhao, S., J. Li, and Y. Li (2015), Dynamics of an interhemispheric teleconnection across the critical latitude through a southerly duct during boreal winter, *J. Clim.*, *28*(19), 7437–7456, doi:10.1175/JCLI-D-14-00425.1.
Zwiers, F. W., and H. von Storch (1995), Taking serial correlation into account in tests of the mean, *J. Clim.*, *8*(2), 336–351, doi:10.1175/1520-0442(1995)008 < 0336:TSCIAI>2.0.CO;2.